Artificial intelligence-enabled automated analysis of transmission electron micrographs to evaluate chemotherapy impact on mitochondrial morphology in triple negative breast cancer

Argenis Arriojas[1,*], Lily M. Baek[2,*], Mariah J. Berner[2], Jiaqi Wang[3], Joseph Duraisingh[4], Alexander Zhurkevich[5], Antentor Othrell Hinton Jr.[6,7], Matthew D. Meyer[8], Lacey E. Dobrolecki[2], Michael T. Lewis[2,9,11], Kourosh Zarringhalam[1,3,#], Gloria V. Echeverria[2,9-11,#]

[1] Center for Personalized Cancer Therapies, University of Massachusetts Boston, Boston, MA, USA

[2] Lester and Sue Smith Breast Center and Department of Medicine, Baylor College of Medicine, Houston, TX, USA

[3] Department of Mathematics, University of Massachusetts Boston, Boston, MA, USA

[4] Department of Cell and Systems Biology, University of Toronto, Toronto, Ontario, Canada

[5] Department of Computer Science, University of Massachusetts Boston, Boston, MA, USA

[6] Department of Molecular Physiology and Biophysics, Vanderbilt University, Nashville, TN, USA

[7] Microscopy and Cell Analysis Core Facility, Mayo Clinic, Rochester, MN, USA

[8] Shared Equipment Authority, Rice University, Houston, TX, USA

[9] Dan L Duncan Comprehensive Cancer Center, Baylor College of Medicine. Houston, TX, USA

[10] Department of Medicine, Baylor College of Medicine, Houston, TX, USA.

[11] Departments of Molecular and Cellular Biology and Radiology. Baylor College of Medicine. Houston, TX, USA

* These authors contributed equally to this work

co-corresponding authors

DISCLOSURES

MTL is a founder and limited partner in StemMed Ltd. and a manager in StemMed Holdings, its general partner. He is a founder and equity stakeholder in Tvardi Therapeutics Inc. Some PDXs are exclusively licensed to StemMed Ltd., resulting in royalty income to MTL. LED is a compensated employee of StemMed Ltd. Some PDXs are exclusively licensed to StemMed Ltd. resulting in royalty income to LED. G.V.E. previously recieved sponsored research funding from Chimerix, Inc. G.V.E. receives

experimental compounds from the Lead Discovery Center of Germany and Jazz Pharmaceuticals, Inc. All other authors have nothing to disclose.

ABSTRACT

Advancements in transmission electron microscopy (TEM) have enabled in-depth studies of biological specimens, offering new avenues to large-scale imaging experiments with subcellular resolution. Mitochondrial structure is of growing interest in cancer biology due to its crucial role in regulating the multi-faceted functions of mitochondria. We and others have established the crucial role of mitochondria in triple-negative breast cancer (TNBC), an aggressive subtype of breast cancer with limited therapeutic options. Building upon our previous work demonstrating the regulatory role of mitochondrial structure dynamics in the metabolic adaptations and survival of chemotherapy-refractory TNBC cells, we sought to extend those findings to a large-scale analysis of transmission electron micrographs. Here we present a U-Net artificial intelligence (AI) model for automatic annotation and assessment of mitochondrial morphology and feature quantification. Our model is trained on 11,039 manually annotated mitochondria across 125 micrographs derived from a variety of orthotopic patient-derived xenograft (PDX) mouse model tumors and adherent cell cultures. The model achieves an F1 score of 0.85 on test micrographs at the pixel level. To validate the ability of our model to detect expected mitochondrial structural changes, we utilized micrographs from mouse primary skeletal muscle cells genetically modified to lack Dynamin-related protein 1 (Drp1). The algorithm successfully detected a significant increase in mitochondrial elongation, in alignment with the well-established role of Drp1 as a driver of mitochondrial fission. Further, we subjected *in vitro* and *in vivo* TNBC models to conventional chemotherapy treatments commonly used for clinical management of TNBC, including doxorubicin, carboplatin, paclitaxel, and docetaxel (DTX). We found substantial within-sample heterogeneity of mitochondrial structure in both *in vitro* and *in vivo* TNBC models and observed a consistent reduction in mitochondrial elongation in DTX-treated specimens. We went on to compare mammary tumors and matched lung metastases in a highly metastatic PDX model of TNBC, uncovering

significant increase in mitochondrial length in metastatic lesions compared to their cognate mammary tumor. This dataset provides high statistical power to detect frequent chemotherapy-induced shifts in mitochondrial shapes and sizes in residual cells left behind after treatment. The successful application of our AI model to capture mitochondrial structure marks a step forward in high-throughput analysis of mitochondrial structures, enhancing our understanding of how morphological changes may relate to chemotherapy efficacy and mechanism of action. Our large, manually curated electron micrograph dataset - now publicly available - serves as a unique gold-standard resource for developing, benchmarking, and applying computational models, while further advancing investigations into mitochondrial morphology and its impact on breast cancer biology.

INTRODUCTION

Mitochondria are multifaceted organelles responsible for energy production through oxidative phosphorylation (OXPHOS). This process generates ATP, the cell's primary energy currency, by utilizing electrons derived from nutrients[1]. Beyond energy production, mitochondria play critical roles in regulating various cellular processes, including apoptosis, cell cycle control, and cell signaling, all of which are dependent on their structural integrity[2-5].

Mitochondrial structure, regulated by their fusion and fission, is highly dynamic. These organelles are enclosed by a double membrane, with the inner membrane folded into cristae that house the OXPHOS machinery[6]. The balance between mitochondrial fusion and fission, governed by key proteins such as dynamin-related protein 1 (DRP1), optic atrophy 1 (OPA1), and mitofusins (MFNs), is crucial for maintaining mitochondrial function and cellular health[7]. In several diseases including cancer, alterations in mitochondrial structure, including those that favor either elongation or fragmentation, are common, contributing to dynamic metabolic reprogramming that supports tumor growth and survival[8-10]. Alterations in mitochondrial fusion and fission can lead to enhanced proliferation, metastasis, or

77 other hallmarks of cancer[9]. Thus, delineating these alterations is critical for gaining a deeper
78 understanding of cancer biology.

79 Triple-negative breast cancer (TNBC) presents significant treatment challenges due to the
80 absence of estrogen and progesterone receptors and human epidermal growth factor receptor two
81 (HER2) amplification or overexpression[11]. Although neoadjuvant (a.k.a pre-surgical) chemotherapy
82 (NACT) with PD-1 immune checkpoint blockers is the standard treatment, approximately half of patients
83 do not achieve complete tumor eradication, leading to significantly elevated risk of metastasis and
84 mortality[12-14]. In our previous studies, we found that after chemotherapy, residual patient-derived
85 xenograft (PDX) tumors which eventually recurred underwent reversible transcriptional and
86 mitochondrial adaptations, with notable increases in OXPHOS-related gene expression and activity
87 relative to treatment-naive tumors[15]. This mitochondrial adaptation was mediated by elevation of the
88 mitochondrial fusion protein OPA1. We also demonstrated that inhibiting OPA1 with the small molecule
89 MYLS22[16] abated mitochondrial fusion, OXPHOS, and chemoresistance[8]. Targeting proteins like DRP1,
90 OPA1, or MFNs could enhance the efficacy of existing treatments and overcome resistance
91 mechanisms, offering new hope for patients with difficult-to-treat cancers[17-20].

92 Electron microscopy is the gold standard method to gain subcellular resolution of organelles.
93 Due to the complexity of mitochondrial structure, accurately quantifying features in imaging data is
94 crucial for understanding the connection between mitochondrial structure and function. Traditionally,
95 analyzing mitochondrial structures involves manually tracing and counting individual mitochondria in
96 electron micrographs to measure morphological parameters such as length, area, circularity, and
97 linearity. This process becomes challenging when the contrast between mitochondria and other
98 organelles or the cytosol is low. In addition, during manual inspection of mitochondria, the examiner
99 often considers only a subset of mitochondria in each image, leading to a loss of information. Individual
100 tumor cells can contain anywhere from a few dozen to several hundred mitochondria, making this
101 manual procedure ineffective for statistically powered high-throughput analysis, as it is extremely time-

102 consuming and may be heavily dependent on examiner bias. These issues can lead to unreliable and
103 inconsistent metrics for quantification, especially considering the extensive intra-tumoral heterogeneity
104 characteristic of most cancers.

105 In recent years, advancements in artificial intelligence (AI), particularly deep machine learning,
106 have transformed image analysis across various medical domains[21-23], including those focused on
107 mitochondrial inner and outer membrane structure[24]. Deep learning models, especially convolutional
108 neural networks, have shown significant success in tasks such as tumor classification, cancer subtype
109 identification, mutation prediction, and treatment outcome prediction using histological images like
110 hematoxylin and eosin (H&E) stained slides[25-27]. These approaches utilize either transfer learning,
111 where pre-trained models are fine-tuned for specific tasks, or full-training strategies that train models
112 from scratch using large domain-specific datasets. Such innovations have enabled the identification of
113 subtle morphological and molecular patterns within images that were previously unnoticed through
114 traditional methods. Similarly, AI-driven approaches have advanced mitochondrial structure studies,
115 enabling precise quantification of mitochondrial dynamics and revealing intricate features like cristae
116 topologies that were difficult to detect. Additionally, pixel-level segmentation of cancer images using
117 autoencoder-based architectures has been adapted for high-resolution segmentation tasks across
118 various image types[28-30]. Among these, U-Net architectures[31] have demonstrated particular efficacy in
119 pixel-level cancer image analysis[25-27,32]. These methods offer automated segmentation and detection
120 capabilities, facilitating more accurate, efficient, and unbiased quantification with exceptional statistical
121 power.

122 In this study, we utilized *in vitro* (adherent cultures of human TNBC cell lines) and *in vivo*
123 (orthotopic PDX mouse models of TNBC) models, in which we previously delineated mitochondrial
124 features and chemotherapeutic responses[15], to conduct a large-scale assessment of mitochondrial
125 morphology. Building on our studies that demonstrated a link between mitochondrial morphology,
126 OXPHOS, and survival in post-chemotherapy residual TNBC cells[8,15], we sought to develop and

127 validate an AI-based approach capable of high-throughput segmentation and quantitative analysis of
128 mitochondrial structures in TNBC. To this end, we first generated a large set of transmission electron
129 micrographs from our models, then curated a high-quality dataset by manually annotating 11,039
130 mitochondria across 125 micrographs from the aforementioned models. These manual annotations
131 served as training data for a U-Net image segmentation model, which was then applied to detect
132 mitochondria at scale. Using computer-vision approaches, we systematically characterized multiple
133 mitochondrial morphological features. This extensive analysis allowed us to statistically quantify
134 sometimes subtle mitochondrial structural upon chemotherapy treatment with exceptional statistical
135 rigor. Here, we describe the extensive training and evaluation of our model, demonstrate its robustness
136 and versatility, and present findings that illuminate how mitochondrial structure adapts in TNBC.

137

138 **RESULTS**

139 **Diverse training datasets to enable robust mitochondrial segmentation**

140 Using our previously established methods to examine residual cells surviving exposure to
141 conventional chemotherapies with *in vivo* and *in vitro* models of TNBC, we systematically collected cell
142 and tumor specimens then subjected them to TEM. We then assembled a diverse training dataset by
143 manually annotating mitochondria from 125 electron micrographs using QuPath[33]. These images
144 ranged in calibrated pixel size from 0.36 to 23 nm/pixel and were collected from two cell culture models
145 – primary mouse skeletal myotubes genetically engineered to lack the mitochondrial fission-driving
146 gene *Drp1* (*Drp1* KO) and human TNBC cells (MDA-MB-231) as well as seven orthotopic patient-
147 derived xenograft (PDX) TNBC models (PIM001-P, PIM005[15], PIM056[34], WHIM-14[35], BCM-2147[36],
148 BCM-15116 (unpublished), and HCI-010[35], each derived from a unique TNBC patient. At an
149 intermediate resolution of 7.5 nm/pixel, slides typically contained between 100 - 500 mitochondria. Data
150 acquisition involved three separate microscopists, each employing unique microscope settings and

capturing various specimens. This diversity in magnification levels, microscope configurations, image formats (including presence of scale bars), and biological systems, helped us build a model that learned to recognize mitochondrial structures under varied conditions. This adaptability is critical for its intended application, as it may allow for accurate predictions irrespective of resolution or experimental setup.

Model development overview

Figure 1 shows a schematic of our pipeline. Briefly, we began with preparation of training data by manually annotated micrographs, followed by tiling at a common resolution (7.5 nm/pixel), then data augmentation to enhance model robustness. A U-Net was trained, allowing the model to learn complex features associated with mitochondrial morphology. The trained model was then utilized to make predictions on new images, detecting and outlining mitochondrial structures. Finally, we performed downstream analyses in two major steps: (1) computer vision tasks (e.g., contour detection, feature characterization such as maximum Feret's diameter and area) and (2) statistical assessments (*e.g.*, distribution measurements) to compare control versus experimental conditions. This streamlined workflow laid the foundation for high-throughput, quantitative evaluation of mitochondrial morphology.

Model performance evaluation

We employed a 5-fold cross-validation approach, using images from each individual dataset as well as an aggregate dataset consisting of mixed images across datasets ("Mixture") (Fig. 2). We assessed F1 scores to determine the consistency and robustness of mitochondrial segmentation performance (Fig. 3). The heatmap reveals variations in F1 scores for each dataset, with the PIM001-P PDX model achieving the highest score on its corresponding test dataset (F1 = 0.86), while *Drp1* KO and HCI-010 reached 0.84 and 0.72, respectively, indicating strong alignment between model predictions and manual annotations (Fig. 3A). By contrast, the *Drp1* KO model shows lower performance on other datasets, with scores of 0.53 on HCI-010 and 0.19 on PIM001-P, indicating that dataset-specific characteristics can strongly influence robustness. Training on the Mixture attenuates

these differences and yields 0.80 on *Drp1* KO, 0.74 on HCI-010, and 0.84 on PIM001-P, providing competitive performance with improved consistency across datasets. This trend is observed in the evaluation of recall, where the Mixture model performs better than single models trained on individual datasets. Given the class imbalance in this segmentation task, precision–recall (PR) curves are the most appropriate evaluation. The PR AUC values are 0.92, 0.80, and 0.94 for the *Drp1* KO, HCI-010, and PIM001-P models, respectively, which align closely with the F1 scores (Fig. 3B).

To further evaluate the model's predictive accuracy, we visually compared the model's segmentation output with manual annotations for sample images across the datasets. Representative images are shown where mitochondria identified by manual annotation (blue) and model prediction (red) are overlaid (magenta) in the "composed" panels, highlighting regions of concordance and minor discrepancies (Fig. 3C). Overall, the model successfully identified the majority of mitochondria, aligning with quantitative results, and demonstrating its ability to reliably detect mitochondrial structure under varied experimental conditions. Despite some challenges in specific datasets, these findings underscore the model's broad applicability for large-scale mitochondrial morphology analysis, particularly when dealing with mixed image sets.

Evaluating alternative model architectures

To explore whether other recently developed segmentation architectures could enhance performance, we trained U-Net++[37] (Mixture++) and Mask R-CNN[38] (Mixture-RCNN) models using the Mixture training dataset and compared it directly with the corresponding U-Net model. As shown in Fig.3A, U-Net++ achieved similar F1 scores but consistently improved recall across all three datasets, indicating a modest advantage in capturing mitochondria pixels that may be missed by the standard U-Net. In contrast, Mask R-CNN shows substantially lower F1 on all test sets and mixed recall. Although U-Net++ offered modest improvements in recall, these gains were not accompanied by meaningful changes in F1 score. Given that our primary analyses were completed using the U-Net architecture

199 with consistent training, benchmarking, and validation across datasets, we opted to retain the U-Net
200 model for subsequent analyses.

201 **Model benchmarking against MitoNet**

202 We compared our dataset-specific U-Net models to the general purpose MitoNet-v1 model [39]
203 using pixel-level F1 score and recall metrics (Fig. 3A). Across all test datasets, our specialized models
204 outperformed MitoNet-v1, achieving higher F1 scores and recall in most cases. Performance was
205 especially improved for PIM001-P and HCI-010 datasets, where the score gap was the largest. These
206 results demonstrate that domain-specific training on TEM images from TNBC models substantially
207 enhanced segmentation accuracy over a general tool.

208 ***In vitro* cell models provide biological validations of the algorithm**

209 We sought biological validation of our model with two approaches. First, we genetically
210 manipulated a canonical mitochondrial structure regulator to test the AI's ability to discern an expected
211 structural difference. Specifically, we conducted TEM of murine skeletal primary cells that were either
212 wild type (WT) or engineered to lack the mitochondrial fission protein Drp1 (*Drp1* KO). Micrographs
213 were analyzed at a resolution of 7.5 nm/pixel. Our data demonstrated a statistically significant increase
214 in elongation (where a value of 1 represents a perfect circle and higher values indicate more elongated
215 shapes) in *Drp1* KO cells compared to WT (Fig. 4B), consistent with the well-established role of Drp1
216 in causing mitochondrial fission. Histograms (Fig. 4C) show a clear rightward shift in elongation for *Drp1*
217 KO relative to WT, with a broader high-elongation tail, consistent with increased mitochondrial
218 elongation. In contrast, the area distributions are largely overlapping and remain skewed toward small
219 objects, in line with the non-significant difference seen in the Fig. 4B. These findings highlight the ability
220 of our model to effectively capture and quantify expected mitochondrial morphological differences.

221 As a second biological validation, we examined micrographs from drug-treated samples for
222 which we had previously established mitochondrial structure alterations using a variety of methods and

223 functional characterizations[8]. We previously reported that different types of standard chemotherapies
224 impacted mitochondrial morphology of TNBC cells in distinct ways: DNA-damaging chemotherapies
225 induced mitochondrial elongation, while taxanes, which disrupt microtubule dynamics, usually reduced
226 mitochondrial elongation (Fig. 5A)[8]. Consistent with those findings, our model detected a significant
227 increase in elongation in MDA-MB-231 TNBC cells treated with DNA-damaging chemotherapies
228 doxorubicin (DXR) or carboplatin (CRB) compared to vehicle (VEH) (Fig. 5B). In contrast, treatment
229 with the taxanes paclitaxel (PTX) or docetaxel (DTX) resulted in decreased mitochondrial elongation
230 and area compared to VEH (Fig.5B). Together, these findings validate our model's ability to detect
231 expected biological changes and highlight its potential for broader discovery applications.

232

233 **Mitochondrial structure changes upon chemotherapy treatment in PDX models**

234 We next sought to investigate whether our approach could detect changes in mitochondrial
235 features, for which we did not have a priori knowledge, during clinically relevant biological transitions in
236 TNBC using orthotopic PDX models. These models are well-known to recapitulate metastatic[40] and
237 therapeutic response[8,15,41] phenotypes that match the originating patient tumors. We treated five unique
238 PDX models, representing five TNBC patients, with the conventional taxane agent DTX, often included
239 as a standard treatment for patients with TNBC. Tumors in the five models exhibited varying degrees
240 of responses to DTX (Fig. 6A), as expected based on heterogeneity of chemotherapy efficacy that is
241 common amongst TNBC patients. We collected mammary tumors from mice that were either untreated
242 (n=1-3 per group) or treated with DTX (n=1-3 per group). Residual DTX tumors were harvested 20-28
243 days after treatment initiation. Tumors were fixed and processed for TEM followed by automated
244 mitochondrial analysis using our algorithm. In three out of five PDX models, we observed decreased
245 mitochondrial elongation following DTX treatment, with BCM-2147 showing a significant reduction
246 ($p<0.0001$). This was accompanied by a decrease in mitochondrial area. Representative micrographs
247 illustrate these findings (Fig. 6C). Additionally, in tumors with greater baseline mitochondrial elongation,

248 we detected a more pronounced reduction in elongation after DTX treatment, suggesting that initial
249 mitochondrial morphology may influence the extent of structural and functional adaptations they
250 undergo (Fig.6D). Indeed, our prior study provided functional evidence that a transition towards
251 mitochondrial fragmentation reduced OXPHOS in TNBC cells[8]. We did not observe any clear
252 association between mitochondrial features and degree of DTX-induced change in tumor volume
253 (Fig.6A-C).

254 **Reproducible mitochondrial elongation in a PDX model of spontaneous lung metastasis**

255 We used a highly metastatic PDX model, PIM056, derived from a treatment-naïve TNBC patient.
256 This model develops multifocal macro-metastatic lung lesions within 16 weeks of mammary fat pad
257 (MFP) engraftment without the need for survival tumor resection surgery. This rapidly aggressive
258 metastatic phenotype is exceedingly rare amongst PDX models. Notably, a prior study using H&E and
259 human-specific mitochondrial immunostaining confirmed that the lung metastases in the PIM056 model
260 are predominantly composed of human tumor cells, rather than mouse stromal tissue, thereby
261 validating the cellular identity of the regions analyzed by TEM[42]. Approximately 16 weeks post
262 engraftment, when the mammary tumors measured on average 1000 mm^3, we collected matched MFP
263 tumors and macro-dissected lung metastases from four individual replicate mice (Fig.7A). TEM followed
264 by automated mitochondria detection revealed significantly longer mitochondria in lung metastases
265 compared to mammary tumors (Fig. 7B-D). In $HER2^+$ breast cancer, brain metastases exhibit increased
266 mitochondrial fission relative to MFP tumors[43]. In TNBC, several studies suggest a greater reliance on
267 mitochondrial OXPHOS in lung metastases than at other metastatic sites[44] ; however, the contribution
268 of mitochondrial dynamics to these differences remains unresolved. The functional relevance of
269 mitochondrial length in TNBC metastasis will be an important topic for future investigations, and our
270 findings highlight the importance of broadening this analysis to additional models of TNBC metastasis.

271 **DISCUSSION**

272 The application of AI is advancing the field of biomedical image analysis[45]. Manual annotation of
273 cancer images is labor-intensive, prone to human bias, and often inconsistent between analysts,
274 platforms, and institutions, making large-scale studies impractical. The AI-driven model presented here
275 addresses these limitations by automating the detection and characterization of mitochondrial
276 morphology with high accuracy and consistency. A key contribution of our AI model is its capacity to
277 capture and quantify the heterogeneity and dynamics of mitochondrial morphology in biologically
278 important transitions within cancer cells.

279 Chemotherapy-induced changes in mitochondrial structure are crucial indicators of cellular
280 adaptive mechanisms, including metabolic reprogramming and resistance to cell death. Notably, our
281 prior work demonstrated that genetically or pharmacologically inducing mitochondrial fission or fusion
282 was sufficient to modulate OXPHOS and chemotherapeutic responses[8]. By detecting subtle changes
283 in structural features across large datasets, our approach provides new insights into how mitochondria
284 may contribute to the survival of residual cancer cells post-treatment. We expect our model and highly
285 curated annotations may not only accelerate the analysis of large datasets but may also enable a level
286 of statistical rigor that is difficult to achieve with manual methods. Its robustness, stemming from training
287 on a diverse set of images, underscores its potential for broad applicability in various biological contexts.
288 To benefit the research community, we have made both our algorithm code and our extensive collection
289 of TEM images publicly available. This dataset includes 125 micrographs with a total of 11,039
290 mitochondrial annotations, which we anticipate will serve as a valuable resource for developing further
291 AI-driven analysis tools.

292 We observed substantial intra-tumor heterogeneity of mitochondrial shapes and sizes within
293 individual micrographs from both cell lines and PDX models (Supplementary Fig. 1). Although genomic,
294 transcriptomic, epigenomic, and proteomic heterogeneity are well-established phenomena across
295 diverse cancers, including within the cell models in this study, diversity of mitochondrial structure has
296 only recently begun to gain attention in cancer[46,47]. Our algorithm's ability to capture this heterogeneity

297 with high resolution, even within a decades-old, well-established human cell line MDA-MB-231,
298 suggests an important, previously underappreciated layer of complexity in cancer cell biology. These
299 observations raise compelling questions about how variations in mitochondrial morphology may
300 correlate with functional differences or therapy responses, underscoring the need for deeper
301 investigation into the potential role of mitochondrial heterogeneity in tumor progression.

302 Our study has several limitations. First, PDX models lack a fully intact immune system, which
303 may be important for mitochondrial features of tumor cells. Consequently, extending our algorithm to
304 immune-competent mouse tumor models will be crucial. Second, the generalizability of our observed
305 chemotherapy-induced mitochondrial structure changes should be further assessed in additional *in vitro*
306 and *in vivo* models with additional conventional chemotherapies, and ideally in human tumor specimens.
307 This is especially important given the well-established inter-patient heterogeneity of TNBC[48-50]. Our
308 algorithm is precisely designed to enable such high-throughput analyses on large sample sets. Third,
309 TEM provides only a two-dimensional cross section of mitochondria and is unable to capture their full
310 three-dimensional complexity[47]. We hypothesize that analyzing high numbers of mitochondria,
311 representing a random sampling of cells' cross-sections, as presented in this study, may mitigate this
312 limitation by approximating the "average" morphological properties within each sample.

313 In our metastasis PDX study, we observed altered mitochondrial elongation reproducibly across
314 four replicate mice when comparing their lung metastases to their cognate MFP tumor. These findings
315 are in line with our prior report of the reproducible clonal bottleneck during the process of metastasis in
316 similar TNBC PDX models, and we conducted analogous experiments in biological replicate mice from
317 that model to uncover reproducible alterations in clonal architecture[40]. The fact that mitochondrial
318 changes arose repeatedly in independent mice suggests potential functional relevance, but that must
319 be rigorously tested in future perturbation experiments in PIM056 and in additional models of metastatic
320 TNBC.

321 We acknowledge that TEM, while providing the gold standard for subcellular resolution of
322 mitochondrial structure, involves intrinsically complex sampling and processing procedures. These
323 include specialized aldehyde fixation, osmium tetroxide post-fixation, resin embedding, ultramicrotomy,
324 and heavy metal counterstaining; procedures that require significantly longer processing times, higher
325 costs, and more advanced technical expertise compared to conventional light microscopy. Despite
326 these practical constraints, TEM remains essential for assessing mitochondrial morphological features
327 that cannot be resolved with light microscopy. While emerging technologies like focused ion beam
328 scanning electron microscopy (FIB-SEM) enable three-dimensional reconstruction of mitochondrial
329 cristae at nanometer resolution, their application remains even more limited, with single-cell
330 acquisitions requiring days to weeks of imaging and processing[51-53], restricting throughput to dozens of
331 mitochondria across only a few cells per experiment. This is almost certainly insufficient for capturing
332 the heterogeneity of cancer cell populations. Our AI-driven approach maximizes the value extracted
333 from TEM images by enabling rapid, unbiased analysis of thousands of mitochondria across our
334 manually curated dataset of 125 micrographs, thereby overcoming the traditional bottleneck of manual
335 annotation while maintaining the resolution necessary to detect morphological changes.

336 While our current analysis focused exclusively on mitochondrial morphology, a more holistic
337 understanding of the chemotherapy-induced cellular changes will require analyzing additional
338 organelles, such as the nucleus, cell membrane, lipid droplets, and endoplasmic reticulum, that can
339 have important interactions with mitochondria. These organelles play significant roles in cellular
340 metabolism, signaling, and homeostasis in concert with mitochondria and may be important
341 contributors to therapeutic resistance in cancer.

342 Several high-quality datasets and segmentation frameworks have advanced the field of
343 mitochondrial and organelle image analysis, including MitoNet, MitoEM, OpenOrganelle, CREMI, and
344 Lucchi[39,54-58]. Each of these resources serves unique purposes. MitoNet provides a generalizable deep-
345 learning framework for mitochondria segmentation across diverse EM datasets. MitoEM and

OpenOrganelle focus on large-scale 3D connectomics data, enabling volumetric reconstruction and detailed mitochondrial network analysis. Meanwhile, the CREMI and Lucchi datasets, though smaller, have served as important benchmarks for EM segmentation methods, often targeting synaptic or nuclear structures alongside mitochondria. Although these tools are invaluable for general benchmarking, they differ substantially from our target application. Most are designed for broad organelle segmentation or 3D volume analysis, typically using isotropic serial-section or FIB-SEM data from non-cancer tissues. By contrast, our pipeline is purpose-built for 2D TEM of TNBC models, with an emphasis on pixel-level morphological quantification of thousands of mitochondria per experiment, enabling the detection of subtle but potentially relevant structural shifts, such as chemotherapy-induced fragmentation or elongation, across large and heterogeneous datasets.

Our rationale for developing a dedicated TNBC-TEM segmentation framework rests on two key points. First, domain-specific optimization was essential, as benchmarking revealed that general-purpose models often underperform on TNBC TEM data due to differences in tissue type, imaging conditions, and structural complexity. Second, our workflow integrates segmentation with downstream morphometric analysis, allowing rigorous statistical comparisons across biological conditions rather than producing masks alone. In this way, our approach complements rather than replaces generalist models, offering a specialized, high-throughput solution for quantitative mitochondrial morphology analysis in clinically relevant cancer models.

We must note that our models were trained exclusively on 2D TEM images from TNBC PDX samples and cell lines, which inherently limits their generalizability. The models are not necessarily expected to produce accurate segmentation predictions for images outside this training domain, such as different cancer types, tissue types, or imaging modalities. Therefore, researchers applying our model to new biological contexts should carefully validate the predictions through manual review, and may need to perform additional fine-tuning or retraining with domain-specific annotations to achieve optimal performance.

FIGURE LEGENDS

Figure 1. Schematic overview of the U-Net AI pipeline for mitochondrial segmentation and analysis. The workflow begins with the preparation of training data, including transmission electron micrographs and manually annotated masks of mitochondria. Images are then rescaled to a common resolution (7.5nm/pixel) and divided into smaller tiles for input into the neural network. Data augmentation, such as rotations, flips, and brightness adjustments, enhances model robustness to image variability. The U-Net architecture, consisting of contracting and expanding paths, is trained to generate segmentation maps from the input image tiles. Following training, the model is used to make predictions on new images, with segmentation masks stitched together for full-image analysis. Downstream analysis includes computer vision tasks for feature quantification and statistical evaluations of mitochondrial morphology across experimental conditions.

Figure 2. Evaluation of model performance using 5-fold cross-validation across datasets. The datasets include *Drp1* KO, HCI-010, PIM001-P, and a mixed dataset combining samples from all groups. The cross-validation approach divided each dataset into five groups, with one group used for testing and the remaining groups for training in each fold. Line plots on the right display F1 scores for each fold during training, demonstrating convergence and model performance across datasets. Consistent F1 score trends across folds indicate reliable segmentation performance, with variations reflecting dataset-specific characteristics. The mixed dataset exhibited robust generalizability, capturing diverse image features and achieving high performance.

Figure 3. Evaluation of segmentation performance and visual comparison of model predictions. (A) Heatmaps showing F1 scores (left) and recall scores (right) for mitochondrial segmentation models trained on individual datasets (*Drp1* KO, HCI-010, PIM001-P), a pooled dataset (Mixture), or enhanced training strategies (Mixture++, Mixture-RCNN), compared against the benchmark model MitoNet-v1.

395 Each row represents the test dataset, and each column represents the training dataset or model. Higher
396 values (darker blue) indicate better performance. (B) Precision–recall curves for models trained on
397 individual datasets (*Drp1* KO, HCI-010, PIM001-P) when tested on their respective datasets. The area
398 under the curve (AUC) is indicated for each model. (C) Representative TEM images showing raw
399 micrographs (left), manual annotations, and mitochondrial segmentation outputs from models trained
400 on individual datasets or mixture-based approaches. Each row represents a different magnification (top:
401 whole cell, middle: subcellular region, bottom: field with multiple cells). Segmented mitochondria are
402 pseudocolored for visualization: manual annotations (blue), model predictions (red), and overlapping
403 regions (magenta).

404 **Figure 4. Genetic validation of model performance.**

405 (A) Representative micrographs from wild-type (WT) and *Drp1* knockout (KO) murine skeletal muscle
406 cells. Images are shown as raw (left) or with model-predicted mitochondrial contours overlaid in red
407 (right). Scale bars, 0.2 μm. (B) Quantification of mitochondrial elongation (left) and area (μm^2) (right) in
408 WT and *Drp1* KO cells. Boxplots display the mean (black dot), median (horizontal line), interquartile
409 range (box), and whiskers extending to 15–85% anchors, ±1.2×IQR. Sample sizes are indicated inside
410 boxes. Data points outside these bounds were excluded as outliers. ****$P < 0.0001$, ns= not significant
411 by pairwise Wilcoxon test. (C) Distribution histograms of mitochondrial elongation (left) and area (right)
412 for WT and *Drp1* KO groups, shown as percent of group.

413 **Figure 5. Pharmacologic validation of model performance.** (A) Representative micrographs from
414 MDA-MB-231 cells were treated with VEH, DXR, CRB, PTX, or DTX. Images are shown as raw (left)
415 or with model-predicted mitochondrial contours overlaid in red (right). (B) Quantification of mitochondrial
416 elongation (left) and area (μm^2) (right). Boxplots display the mean (black dot), median (horizontal line),
417 interquartile range (box), and whiskers extending to 15–85% anchors, ±1.2×IQR. Sample sizes are
418 indicated inside boxes. Data points outside these bounds were excluded as outliers. ****$P < 0.0001$,
419 ***$P < 0.001$, **$P < 0.01$, *$P < 0.05$, ns= not significant by pairwise Wilcoxon test.

420 **Figure 6. Analysis of mitochondrial changes in PDX models treated with DTX.** (A) Line plots
421 showing normalized tumor volume over time in five PDX models treated with DTX (orange) (starting on
422 Day 0) compared to untreated controls (UNT, blue). Red arrows on the x-axis indicate each DTX
423 administration (*i.p.*, 20mg/kg). (B-C) Box plots summarize mitochondrial elongation (B) and area (C)
424 across the five PDX models. Boxplots display the mean (black dot), median (horizontal line),
425 interquartile range (box), and whiskers extending to 15–85% anchors, ±1.2×IQR. Sample sizes are
426 indicated inside boxes. Data points outside these bounds were excluded as outliers. ****$P < 0.0001$,
427 ***$P < 0.001$, **$P < 0.01$, ns= not significant by pairwise Wilcoxon test. (C) Representative micrographs
428 from BCM-2147 untreated (top) or treated with DTX (bottom). Images are shown as raw (left) or with
429 model-predicted mitochondrial contours overlaid in red (right). Scale bars, 0.2 μm. (E) Scatter plot
430 showing baseline elongation in the untreated (UNT) group (x-axis) vs the percent change (Δ%) in
431 elongation after DTX (y-axis), defined as $(DTX_{mean}-UNT_{mean})/UNT_{mean} \times 100$. Each point represents one
432 model. Colors correspond to the legend. The red dashed line indicates the linear regression fit (P=0.14),
433 and the black dashed line marks no change.

434 **Figure 7. Mitochondrial morphology differences between mammary tumors and lung**
435 **metastases** (A) Schematic representation of the PIM056 PDX model, where tumors were allowed to
436 grow for 16 weeks before isolation of both primary mammary fat pad (MFP) tumors and lung metastases
437 (Lung) for analysis. (B) Representative TEM images show mitochondrial structures in MFP (top) and
438 lung metastases (bottom). Images are shown as raw (left) or with model-predicted mitochondrial
439 contours overlaid in red (right). Scale bars=0.2 μm. (C) Quantification of mitochondrial elongation (top)
440 and area (μm^2) (bottom) in MFP and lung metastases. Boxplots display the mean (black dot), median
441 (horizontal line), interquartile range (box), and whiskers extending to 15–85% anchors, ±1.2×IQR with
442 sample sizes indicated for each group. Data points outside these bounds were excluded as outliers.
443 ****$P < 0.0001$ by pairwise Wilcoxon test. (D) Distribution histograms of mitochondrial elongation (top)
444 and area (bottom) for MFP and lung metastases, shown as percent of group.

445 **Supplementary Figure 1. Mitochondrial elongation and area distributions reveal model-specific**
446 **differences in morphology and heterogeneity under control conditions.**

447 (A) Histograms of mitochondrial elongation and area across control samples (untreated conditions)
448 show distinct distribution patterns across TNBC models. (B) Density ridge plots provide an overview of
449 distribution shapes. (C) Heterogeneity in mitochondrial morphology was quantified using the coefficient
450 of variation (CV) and interquartile range (IQR) for elongation and area.

451

452 **METHODS**

453 **TNBC cell culture and drug treatment**

454 The MDA-MB-231 cell line was purchased directly from ATCC (American Type Culture Collection)
455 and cultured in RPMI-1640 (Gibco, 11879020) supplemented with 5 mM glucose (Gibco, A2494001),
456 10% fetal bovine serum (FBS) (R&D, S11550), and 1× antibiotic-antimycotic solution (Corning, 30-004-
457 CI). Except for carboplatin (solutions were freshly prepared from powder), we prepared stock solutions
458 of 10 mM in DMSO, and further dilutions were prepared in a proper growth medium. Cells were seeded
459 at ~20% confluence and maintained for 48 h before treatment. Cells were then treated with: doxorubicin
460 (final conc. at 100 nM, Sigma-Aldrich, 44583, protected from light), carboplatin (final conc. at 100 μM,
461 Selleck Chemicals, S1215), paclitaxel (final conc. at 10 nM, Selleck Chemicals, Houston TX, S1150) or
462 docetaxel (final conc. at 5 nM, Selleck Chemicals, Houston TX, S1148) for 48 hours before fixation.

463

464 **Authentication of cell lines and PDX models**

465 Cell cultures were tested for mycoplasma contamination each quarter using PCR with the
466 Universal Mycoplasma Detection Kit (ATCC, 30-1012K), and were confirmed to be mycoplasma-free
467 throughout the duration of this study. Short-tandem repeat (STR) DNA fingerprinting was performed on

468 DNA extracted from both cell lines and PDX model tumors by the Cytogenetics and Cell Authentication
469 Core (CCAC) at M.D. Anderson Cancer Center. The Promega 16 High Sensitivity STR Kit (Catalog #
470 DC2100) was used for the fingerprinting analysis, and the resulting profiles were compared against
471 online search databases (DSMZ, ATCC, JCRB, RIKEN) for authentication.

472

473 **Animal studies**

474 This study was carried out in accordance with the *Guide for the Care and Use of Laboratory*
475 *Animals* from the National Institutes of Health (NIH) IACUC. The protocol was approved by the IACUC
476 at BCM (protocol AN-8243 and AN-2289). Mice were euthanized when they reached defined study or
477 ethical end points. Euthanasia was conducted as recommended by the Association for Assessment
478 and Accreditation of Laboratory Animal Care International. PIM001-P, PIM005[15] and PIM056[34] were
479 propagated as previously described[1]. Briefly, cryo-preserved PDX cell suspensions were quickly
480 thawed, then washed with Dulbecco's modified Eagle's medium (DMEM):F12 (Cytiva HyClone,
481 SH30023.01) supplemented with 5% FBS. Viable cells were counted by staining with AOPI dye
482 (Nexcelom Bioscience, CS2-0106) on a Cellometer K2 (Nexcelom Bioscience). For injection into
483 mammary glands, 0.5-1.0 million viable tumor cells were suspended in a total of 20 µl (1:1 volume
484 mixture of medium and Matrigel (Corning, 354234). Suspensions were then immediately injected
485 unilaterally into the fourth mammary fat pads of 5 to 8-week-old female NOD/SCID [NOD.CB17-
486 Prkdc^{scid}/NcrCrl, Charles River, National Cancer Institute (NCI) Colony] or NRG [NOD-Rag1null
487 IL2rgnull] mice (Envigo). For HCI-010, BCM-2147, BCM-15116, and WHIM-14, cryo-preserved tumor
488 fragments (1-2mm^3) were quickly thawed and washed with DMEM. The tumor chunks were
489 orthotopically xenografted to 4th mammary gland of 6-8-week-old SCID/beige female mice.

490 Chemotherapy treatment of PDX models was conducted as previously described. Docetaxel
491 solutions were administered by intraperitoneal injection at 20 mg/kg.

492 For PIM056 metastasis studies, lung metastases and mammary tumors were collected
493 immediately following euthanasia when primary tumors reached approximately 1200 mm^3. Macro-
494 metastatic lesions visual to the naked eye were isolated with scalpels then preserved for TEM as below.

495 To generate *Drp1* KO skeletal muscle murine myotubes, mouse husbandry was carried out in
496 accordance with standard protocols[59] approved by the University of Iowa IACUC. Male C57Bl/6J mice
497 were housed at 22 °C with a 12 h light, 12 h dark cycle and free access to water and standard chow.
498 Controls represent pure C57Bl/6J genetic background mice. In accordance with previous studies[60-62],
499 Tamoxifen-inducible, skeletal muscle-specific *Drp1* KO mice were generated by crossing mice carrying
500 a homozygous floxed allele of *Drp1* with mice carrying a tamoxifen-inducible Cre recombinase under
501 the control of the skeletal muscle-specific myogenin promoter (Jackson Lab).

502

503 **Isolation of satellite cells and differentiation**

504 To collect tissue samples from wild-type or *Drp1* KO mice, animals were anesthetized using
505 isoflurane at 8–10 weeks old. Skeletal muscles from the gastrocnemius and quadriceps were excised
506 and washed twice with 1x phosphate-buffered saline (PBS) supplemented with 1% penicillin-
507 streptomycin and 0.3% fungizone (300 µL/100 mL The muscles were then incubated in Dulbecco's
508 Modified Eagle's Medium (DMEM)-F12 containing 0.2% collagenase II (2 mg/mL), 1% penicillin-
509 streptomycin, and 0.3% fungizone (300 µL/100 mL). Samples were shaken for 90 minutes at 37 °C.
510 Following incubation, the media was removed, and the muscle tissue was washed four times with PBS.
511 The media was then replaced with DMEM-F12 containing 0.05% collagenase II (0.5 mg/mL), 1%
512 penicillin-streptomycin, and 0.3% fungizone (300 µL/100 mL), followed by shaking for 30 minutes at
513 37 °C. Post-digestion, the tissue was ground until cells were dislodged from the tissue matrix and then
514 passed through a 70 µm cell strainer. The isolated cells were centrifuged, resuspended, and plated on
515 BD Matrigel-coated dishes. Adherent cells were differentiated into myotubes by adding DMEM-F12, 20%

516 FBS, 0.004% (40 ng mL-1) basic fibroblast growth factor (R&D Systems, 233-FB/CF), 1× non-essential
517 amino acids, 0.14 × 10^3 m β-mercaptoethanol, 1x penicillin/streptomycin, and 0.3% fungizone (300
518 μL/100 mL). Myotubes were maintained in a medium containing 0.001% (10 ng/mL) growth factor until
519 reaching 85% confluency, then were differentiated in DMEM-F12, 2% FBS, and 1× insulin-transferrin-
520 selenium.

521

522 **Transmission electron microscopy (TEM)**

523 Tumor cells were fixed, processed, and embedded in situ to prevent morphological damage, as
524 follows. Cells were fixed for 24 hours in Karnovsky's fixative, post-fixed in 1% osmium tetroxide,
525 dehydrated in graded ethanol, and embedded in EMbed 812 resin. Ultra-thin sections were cut using a
526 Leica UC7 ultramicrotome, stained with saturated methanolic uranyl acetate and Reynold's lead citrate,
527 and imaged using a JEOL JEM-1230 TEM equipped with an AMT NanoSprint15 sCMOS camera. For
528 tumor tissues, immediately following ethical animal euthanasia, mammary tumors were resected from
529 mice and a ~1 mm-tick tumor slice was placed in Trump's fixation solution and fixed for 24 hours at
530 room temperature with rocking. The necrotic areas that usually found in the core region of solid tumors
531 were avoided. The initial fixed samples then were post-fixed in 1% buffered osmium tetroxide,
532 dehydrated in graded ethanol, and embedded in Polybed 812 resin. Ultra-thin sections were obtained
533 using a Leica UC 7 and sections were stained in 1% aqueous uranyl acetate and Reynold's lead
534 citrate. Images were obtained using a FEI Tecnai Spirit TEM equipped with an Eagle camera and FEI
535 Tia image acquisition software. Approximately 65 images at magnifications of 400-5000x were taken
536 per tumor sample.

537 Myotubes were processed for TEM in accordance with previous studies[63,64]. For 1 h, cells were
538 fixed by incubating at 37 °C with 2.5% glutaraldehyde in 0.1 m sodium cacodylate buffer. After rinsing

539 twice with 0.1 m sodium cacodylate buffer, samples were fixed again at room temperature for 30 min
540 to 1 h using 1% osmium tetroxide and 1.5% potassium ferrocyanide in 0.1 m sodium cacodylate buffer.
541 After secondary fixation, samples were washed for 5 min with 0.1 m sodium cacodylate buffer (7.3 pH).
542 From there, two washings of 5 min with diH_2O ensured the plates were cleaned. While keeping all
543 solutions and plates at room temperature, the samples were incubated with 2.5% uranyl acetate, diluted
544 with H_2O, at 4 °C overnight. Following this, samples were dehydrated using an ethanol gradient series.
545 After dehydration, the ethanol was replaced with Eponate 12 mixed in 100% ethanol in a 1:1 solution,
546 then incubated at room temperature for 30 min. This was repeated three times for 1 h using 100%
547 Eponate 12. The plates were finally placed in new media and cured in an oven at 70 °C overnight.

548 Plates were cracked upon hardening, and the cells were separated by submerging the plate in
549 liquid nitrogen. An 80 nm thickness jeweler's saw was used to cut the block to fit in a Leica UC6
550 ultramicrotome sample holder. From there, the section was placed on formvar-coated copper grids.
551 These grids were counterstained in 2% uranyl acetate for 2 min. Then these grids were counterstained
552 by Reynold's lead citrate for 2 min. Images were acquired by TEM on either a JEOL JEM-1230,
553 operating at 120 kV, or a JEOL 1400, operating at 80 kV.

554

555 **Manual annotation of micrographs**

556 For each tumor or cell line, 50-60 transmission electron micrographs were obtained at different
557 magnifications, ranging from 1000X to 5000X magnification. These micrographs were then loaded into
558 the QuPath software[33], a versatile tool for bioimage analysis. Each mitochondrion within the
559 micrographs was manually annotated using the drawing tool provided by QuPath. This process involved
560 carefully outlining the boundaries of individual mitochondria to ensure precise and accurate
561 characterization of their morphological features. The manual annotations were subsequently used for

562 further analysis, providing a detailed dataset for evaluating mitochondrial structure across various tumor
563 samples.

564

565 **Model**

566 A U-Net model was utilized to perform semantic segmentation on the TEM images. This deep-
567 learning model is an autoencoder that consists of a feature extraction stage (contracting path, encoder)
568 and a reconstruction stage (expansive path, decoder). The model uses a series of convolutional and
569 max pooling layers to transform the input image into abstract features in a latent space, that will then
570 be decoded in the reconstruction stage to match the model output with the corresponding training mask.
571 A defining characteristic of a U-Net model is the use of feature maps from the contracting path, as input
572 features in the expansive path. This choice helps to localize and assemble a more precise output
573 mask[31]. The network architecture is described in the following. The 2D input layer is followed by a
574 Gaussian Noise layer with standard deviation of 0.01. Each convolutional layer has kernel size 3 and
575 is followed by a leaky ReLu activation layer, a 2D spatial dropout layer (rates 0.2 and 0.1 in the
576 contracting and expansive paths respectively), and a batch normalization layer. A convolutional block
577 is composed of two such convolutional layers, followed by either a 2 by 2 max pooling layer in the
578 contracting path, or a 2 by 2 up-convolution layer with stride 2 in the expanding path. The model is
579 composed of 9 convolutional blocks in total: 4 in the contracting path, 1 in the bottleneck, and 4 in the
580 expansive path. The first convolutional block uses 16 filters in each of its convolutional layers. The
581 number of filters used in the convolutional layers doubles after each max pooling layer, and halves after
582 each up-convolution layer. The full model has just under 2 million trainable parameters.

583

584 **Datasets**

585 Three different datasets were used for training four U-Net models. The datasets are labeled as
586 *Drp1* KO, HCI-010, and PIM001-P, with 26, 21, and 37 images respectively. The *Drp1* KO dataset
587 contains images from the control set of an *in vitro* genetically engineered mouse myotube model. HCI-
588 010 and PIM001-P contain images from two corresponding *in vivo* PDX mouse models. All images in
589 the training datasets correspond to non-perturbed (control/vehicle) samples. For each dataset, a model
590 was trained. A mixed model was also trained using images from these three datasets, along with control
591 images of 3 other datasets (BCM-2147, MDA-MB-231, and PIM005), using a total of 125 images for
592 training.

593

594 **Preprocessing training data**

595 The training dataset consists of electron micrographs, each paired with a manually annotated
596 segmentation mask indicating the mitochondria. Magnification information was parsed from the image
597 to obtain the calibrated pixel size. Prior to training or inference, images were scaled to match a common
598 pixel size of 7.5 nm/pixel. Each image-mask pair was tiled to appropriately sized input samples that fit
599 the model architecture shape (444 by 444 in the input layer, and 260 by 260 pixels at the output). The
600 tiled process was performed in an overlapping fashion with a stride of 130 pixels in both horizontal and
601 vertical directions. To avoid losing the pixels at the border, the images were zero-padded. The pixel
602 values are rescaled to lie in the range [0,1]. The tile sets were converted into TF records to improve
603 training computational performance. The final output was assembled by stitching the overlapping
604 predicted mask tiles and taking the average for the overlapping regions.

605

606 **Data augmentation**

607 During model training, the input tiles were randomly transformed by rotating and flipping the
608 images. This step was performed to increase the number of training samples and to avoid orientation

bias. Moreover, the brightness, contrast and gamma image parameters were randomly adjusted to account for variation of these parameters across the input images. Additionally, images were randomly magnified to boost the robustness of the model to input image resolution.

Model training

The model was trained on Nvidia DGX-A100 GPUs, for a total of 1200 epochs and batch size 128. The Adam optimizer was used with the default parameters, and a weighted binary cross entropy loss function, assigning double weight to positive mask pixels. Model checkpoints were saved for the best achieved loss on the validation sets. The convergence of the model was monitored using the corresponding loss metric, as well as the IOU and DICE coefficients.

Performance evaluation

The data was split into a training set and a test set (85% and 15% approximately). A 5-fold cross validation was used in the training set, where each fold uses 4 subsets for training and the remaining 5th set as validation. Model performance was assessed using the left-out test set.

Model predictions

Each of the 5 resulting models from the cross-validation procedure were used to make predictions on new images. An ensemble approach was used to aggregate the results in a single prediction, by taking the average of all predictions. Since the semantic segmentation models are optimized for analysis at a calibrated pixel size of 7.5 nm/pixel, input images are scaled to this magnification prior inference, and predictions are scaled back to the original size.

Assesing alternative model architectures

Our U-Net implementation was extended to the more recent U-Net++ architecture to evaluate whether its enhanced skip connections could improve segmentation performance. The model was constructed using the same parameters as the standard U-Net, resulting in approximately 2.4 million parameters in total, a ~25% increase compared to the original architecture.

We also evaluated a general-purpose instance segmentation framework, Detectron2's COCO-pretrained Mask R-CNN (mask_rcnn_R_50_FPN_3x, Meta AI), to assess whether this architecture could offer improvements over our U-Net-based models. For compatibility, the ground truth annotations from our Mixture training dataset were prepared following Detectron2's requirements, converted from semantic masks into COCO-style JSON format containing per-instance metadata such as contour coordinates and instance IDs, and registered in Detectron2 as a new local dataset. Model inference was performed via a tile-wise pipeline (512 by 512 px tiles with 20% overlap), followed by stitching to full resolution and rasterizing instance predictions into semantic masks. Despite its versatility, the Mask R-CNN baseline did not outperform our domain-specific U-Net models on the test datasets.

Benchmarks

To benchmark our model's performance, we compared it against MitoNet_v1[39], a widely-used mitochondria segmentation tool. The comparison was performed using the Empanada wrapper (v1.2) integrated with Napari (v0.4.18) in a Python 3.9 conda environment. We applied MitoNet's 2D inference tool with default parameters to 13 test images from our dataset, generating instance segmentation masks for mitochondria in each image. To enable direct comparison with our U-Net predictions, the instance segmentation masks were converted to semantic segmentation format by flattening individual mitochondria masks using Napari's "convert to image" feature. Model performance was quantified using pixel-level F1 score and recall metrics.

656

657 **Postprocessing for morphometric analysis**

658 For morphological measurements, predicted binary masks were first smoothed to reduce single-
659 pixel noise and produce cleaner object boundaries. This was achieved by repeated convolution with a
660 normalized 2D Gaussian kernel (sigma = 5 nm in image space) for 24 iterations, followed by by re-
661 thresholding to recover a binary mask. This smoothing step was applied uniformly to all predictions
662 prior to morphometric quantification, and was not used in the calculation of segmentation performance
663 metrics.

664

665 **Statistical analysis**

666 For each group, data are summarized as the median, mean (black dot in boxplots), interquartile
667 range (IQR), and whiskers spanning the 15th–85th percentiles with ±1.2×IQR, unless otherwise noted.
668 Differences between groups were assessed using the Wilcoxon rank-sum test (two-sided) because the
669 distributions of elongation and area are non-Gaussian, highly skewed, and contain unequal variances
670 and outlier structures.

671

672 **Data and code availability**

673 Cell line models of TNBC are available for purchase from ATCC. PDX models can be made
674 available to investigators through a material transfer agreement with the University of Texas MD
675 Anderson Cancer Center (PIM001-P, PIM005 and PIM056) or Baylor College of Medicine (HCI-010,
676 BCM-2147, BCM-15116, and WHIM-14). The Python code will be made available on GitHub (DOI
677 pending). Electron micrographs and annotated mitochondrial masks are deposited in Bioimage
678 Archive[65] under accession # S-BIAD2271.

AUTHOR CONTRIBUTIONS

A.A., L.M.B., K.Z., and G.V.E were responsible for overall completion of the study, writing the manuscript, and preparation of figures.

L.M.B., K.Z., and G.V.E were responsible for project conceptualization.

L.M.B. conducted PDX and cell line experiments, generated electron micrographs, conducted manual annotations of mitochondria, and data analyses under the supervision of G.V.E.

A.A. conducted computational algorithm development, optimization, and testing under the supervision of K.Z.

M.J.B. conducted PDX chemotherapy trials and generated electron micrographs analyzed in this study under the supervision of G.V.E.

A.Z. conducted initial algorithm development under the supervision of K.Z.

J.W. and J.D. contributed to the benchmarking efforts. J.W. performed training and evaluation for the Mixture-RCNN model. J.D. performed model evaluations for the MitoNet-v1 segmentation model.

A.O.H. provided electron micrographs of WT and *Drp1*KO myotubes.

Jiaqi Wang[3], Joseph Duraisingh

JW implemented the Mask-RCNN model and performed benchmark analysis.

JD implemented MitoNet and Empanada benchmakrs.

M.D.M. aided in design of electron microscopy imaging and generated most images in this study.

L.E.D. conducted PDX chemotherapy trials and provided tissues for electron microscopy under the supervision of M.T.L.

ACKNOWLEDGEMENTS

We are grateful to the breast cancer patients who donated their biopsies for cell line and PDX model generation. We are grateful to Mrs. Janice Cowden for providing advocacy support for our research. Dr. James P. Barrish assisted with TEM. Dr. Junegoo Lee assisted with mouse experiments. Dr. Helen Piwnica-Worms provided the PIM001-P and PIM056 PDXs through MTA with the University of Texas MD Anderson Cancer Center, and model generation was supported by a generous gift from the Cazalot Foundation through the MD Anderson Women's Cancer Moonshot Program. STR DNA fingerprinting was done by the Cytogenetics and Cell Authentication Core at M.D. Anderson Cancer Center.

FUNDING

G.V.E. is a Cancer Prevention Research Institute of Texas (CPRIT) Scholar in Cancer Research. The authors are supported by CPRIT RR200009 to G.V.E., National Institutes of Health (NIH) R37CA269783-01A1 to G.V.E., R37CA269783-01A1 to K.Z., R01AI167570 to K.Z., American Cancer Society RSG-22-093-01-CCB to G.V.E, National Science Foundation 2140736 to M.J.B., and Baylor Research Advocates for Student Scholars (BRASS) Myra Branum Wilson Scholarship to M.J.B. The content is solely the responsibility of the authors and does not necessarily represent the official views of the NIH, NSF, CPRIT, ACS, or BRASS. The BCM PDX core is supported by P30 Cancer Center Support Grant NCI-CA125123, CPRIT Core Facilities Support Grant RP220646.

REFERENCES CITED

1 Anderson, A. J., Jackson, T. D., Stroud, D. A. & Stojanovski, D. Mitochondria-hubs for regulating cellular biochemistry: emerging concepts and networks. *Open Biol* **9**, 190126, doi:10.1098/rsob.190126 (2019).

2 Rossmann, M. P., Dubois, S. M., Agarwal, S. & Zon, L. I. Mitochondrial function in development and disease. *Dis Model Mech* **14**, doi:10.1242/dmm.048912 (2021).

3 Nguyen, T. T. *et al.* Mitochondria-associated programmed cell death as a therapeutic target for age-related disease. *Exp Mol Med* **55**, 1595-1619, doi:10.1038/s12276-023-01046-5 (2023).

4 Mitra, K., Wunder, C., Roysam, B., Lin, G. & Lippincott-Schwartz, J. A hyperfused mitochondrial state achieved at G1-S regulates cyclin E buildup and entry into S phase. *Proc Natl Acad Sci U S A* **106**, 11960-11965, doi:10.1073/pnas.0904875106 (2009).

5 Egan, G. *et al.* Mitochondrial and Metabolic Pathways Regulate Nuclear Gene Expression to Control Differentiation, Stem Cell Function, and Immune Response in Leukemia. *Cancer Discov* **11**, 1052-1066, doi:10.1158/2159-8290.CD-20-1227 (2021).

6 Chen, W., Zhao, H. & Li, Y. Mitochondrial dynamics in health and disease: mechanisms and potential targets. *Signal Transduct Target Ther* **8**, 333, doi:10.1038/s41392-023-01547-9 (2023).

7 Raven, K. D. & Kapetanovic, R. Mitochondrial dynamics: Regulating cell metabolism, homoeostasis, health and disease. *Semin Cell Dev Biol* **161-162**, 20-21, doi:10.1016/j.semcdb.2024.02.002 (2024).

8 Baek, M. L. *et al.* Mitochondrial structure and function adaptation in residual triple negative breast cancer cells surviving chemotherapy treatment. *Oncogene* **42**, 1117-1131, doi:10.1038/s41388-023-02596-8 (2023).

9 Boulton, D. P. & Caino, M. C. Mitochondrial Fission and Fusion in Tumor Progression to Metastasis. *Front Cell Dev Biol* **10**, 849962, doi:10.3389/fcell.2022.849962 (2022).

10 Sessions, D. T. *et al.* Opa1 and Drp1 reciprocally regulate cristae morphology, ETC function, and NAD(+) regeneration in KRas-mutant lung adenocarcinoma. *Cell Rep* **41**, 111818, doi:10.1016/j.celrep.2022.111818 (2022).

11 Perou, C. M. Molecular stratification of triple-negative breast cancers. *Oncologist* **16 Suppl 1**, 61-70, doi:10.1634/theoncologist.2011-S1-61 (2011).

12 Symmans, W. F. *et al.* Long-Term Prognostic Risk After Neoadjuvant Chemotherapy Associated With Residual Cancer Burden and Breast Cancer Subtype. *J Clin Oncol* **35**, 1049-1060, doi:10.1200/JCO.2015.63.1010 (2017).

13 Yau, C. *et al.* Residual cancer burden after neoadjuvant chemotherapy and long-term survival outcomes in breast cancer: a multicentre pooled analysis of 5161 patients. *Lancet Oncol* **23**, 149-160, doi:10.1016/S1470-2045(21)00589-1 (2022).

14 Hamy, A. S. *et al.* Prognostic value of the Residual Cancer Burden index according to breast cancer subtype: Validation on a cohort of BC patients treated by neoadjuvant chemotherapy. *PLoS One* **15**, e0234191, doi:10.1371/journal.pone.0234191 (2020).

15 Echeverria, G. V. *et al.* Resistance to neoadjuvant chemotherapy in triple-negative breast cancer mediated by a reversible drug-tolerant state. *Sci Transl Med* **11**, doi:10.1126/scitranslmed.aav0936 (2019).

16 Herkenne, S. & Scorrano, L. OPA1, a new mitochondrial target in cancer therapy. *Aging (Albany NY)* **12**, 20931-20933, doi:10.18632/aging.104207 (2020).

17 Xie, L. *et al.* Drp1-dependent remodeling of mitochondrial morphology triggered by EBV-LMP1 increases cisplatin resistance. *Signal Transduct Target Ther* **5**, 56, doi:10.1038/s41392-020-0151-9 (2020).

18 Alalawy, A. I. *et al.* Inhibition of Drp1 orchestrates the responsiveness of breast cancer cells to paclitaxel but insignificantly relieves paclitaxel-related ovarian damage in mice. *Sci Rep* **13**, 22782, doi:10.1038/s41598-023-49578-0 (2023).

19 Noguchi, M. *et al.* Inhibition of the mitochondria-shaping protein Opa1 restores sensitivity to Gefitinib in a lung adenocarcinomaresistant cell line. *Cell Death Dis* **14**, 241, doi:10.1038/s41419-023-05768-2 (2023).

20 Decker, C. W. *et al.* Mitofusin-2 mediates doxorubicin sensitivity and acute resistance in Jurkat leukemia cells. *Biochem Biophys Rep* **24**, 100824, doi:10.1016/j.bbrep.2020.100824 (2020).

21 Rub, J. *et al.* A deep-learning tool for species-agnostic integration of cancer cell states. *bioRxiv*, 2024.2012.2020.629285, doi:10.1101/2024.12.20.629285 (2024).

22 Chaudhry, F., Kim, T. W., Elemento, O. & Betel, D. Machine learning analysis of population-wide plasma proteins identifies hormonal biomarkers of Parkinson's Disease. *medRxiv*, doi:10.1101/2024.12.21.24313256 (2024).

23 Wang, J. M. *et al.* Deep learning integrates histopathology and proteogenomics at a pan-cancer level. *Cell Rep Med* **4**, 101173, doi:10.1016/j.xcrm.2023.101173 (2023).

24 Suga, S. *et al.* An interactive deep learning-based approach reveals mitochondrial cristae topologies. *PLoS Biol* **21**, e3002246, doi:10.1371/journal.pbio.3002246 (2023).

25 Jiang, Y., Yang, M., Wang, S., Li, X. & Sun, Y. Emerging role of deep learning-based artificial intelligence in tumor pathology. *Cancer Commun (Lond)* **40**, 154-166, doi:10.1002/cac2.12012 (2020).

26 Noorbakhsh, J. *et al.* Deep learning-based cross-classifications reveal conserved spatial behaviors within tumor histological images. *Nat Commun* **11**, 6367, doi:10.1038/s41467-020-20030-5 (2020).

27 Yang, Y., Fang, Q. & Shen, H. B. Predicting gene regulatory interactions based on spatial gene expression data and deep learning. *PLoS Comput Biol* **15**, e1007324, doi:10.1371/journal.pcbi.1007324 (2019).

28 Rich, J. M. *et al.* Deep learning image segmentation approaches for malignant bone lesions: a systematic review and meta-analysis. *Front Radiol* **3**, 1241651, doi:10.3389/fradi.2023.1241651 (2023).

29 Xu, Y. *et al.* Advances in Medical Image Segmentation: A Comprehensive Review of Traditional, Deep Learning and Hybrid Approaches. *Bioengineering (Basel)* **11**, doi:10.3390/bioengineering11101034 (2024).

30 Yuan, J. Brain tumor image segmentation method using hybrid attention module and improved mask RCNN. *Sci Rep* **14**, 20615, doi:10.1038/s41598-024-71250-4 (2024).

31 Ronneberger, O., Fischer, P. & Brox, T. 234-241 (Springer International Publishing).

32 Farahmand, S. *et al.* Deep learning trained on hematoxylin and eosin tumor region of Interest predicts HER2 status and trastuzumab treatment response in HER2+ breast cancer. *Mod Pathol* **35**, 44-51, doi:10.1038/s41379-021-00911-w (2022).

33 Bankhead, P. *et al.* QuPath: Open source software for digital pathology image analysis. *Sci Rep* **7**, 16878, doi:10.1038/s41598-017-17204-5 (2017).

34 Echeverria, G. V. *et al.* Predictors of success in establishing orthotopic patient-derived xenograft models of triple negative breast cancer. *NPJ Breast Cancer* **9**, 2, doi:10.1038/s41523-022-00502-1 (2023).

35 Guillen, K. P. *et al.* A human breast cancer-derived xenograft and organoid platform for drug discovery and precision oncology. *Nat Cancer* **3**, 232-250, doi:10.1038/s43018-022-00337-6 (2022).

36 Zhang, X. *et al.* A renewable tissue resource of phenotypically stable, biologically and ethnically diverse, patient-derived human breast cancer xenograft models. *Cancer Res* **73**, 4885-4897, doi:10.1158/0008-5472.CAN-12-4081 (2013).

37 Zhou, Z., Siddiquee, M. M. R., Tajbakhsh, N. & Liang, J. UNet++: A Nested U-Net Architecture for Medical Image Segmentation. *Deep Learn Med Image Anal Multimodal Learn Clin Decis Support (2018)* **11045**, 3-11, doi:10.1007/978-3-030-00889-5_1 (2018).

38 Kaiming He, G. G., Piotr Dollár, Ross Girshick. Mask R-CNN. *arXiv* doi:https://doi.org/10.48550/arXiv.1703.06870 (2017).

39 Conrad, R. & Narayan, K. Instance segmentation of mitochondria in electron microscopy images with a generalist deep learning model trained on a diverse dataset. *Cell Syst* **14**, 58-71 e55, doi:10.1016/j.cels.2022.12.006 (2023).

40 Echeverria, G. V. *et al.* High-resolution clonal mapping of multi-organ metastasis in triple negative breast cancer. *Nat Commun* **9**, 5079, doi:10.1038/s41467-018-07406-4 (2018).

41 Lei, J. T. *et al.* Patient-Derived Xenografts of Triple-Negative Breast Cancer Enable Deconvolution and Prediction of Chemotherapy Responses. *bioRxiv*, doi:10.1101/2024.12.09.627518 (2025).

42 Rinkenbaugh, A. L. *et al.* An Annotated Biobank of Triple-Negative Breast Cancer Patient-Derived Xenografts Features Treatment-Naive and Longitudinal Samples During Neoadjuvant Chemotherapy. *Cancer Res*, doi:10.1158/0008-5472.CAN-24-5023 (2025).

43 Parida, P. K. *et al.* Limiting mitochondrial plasticity by targeting DRP1 induces metabolic reprogramming and reduces breast cancer brain metastases. *Nat Cancer* **4**, 893-907, doi:10.1038/s43018-023-00563-6 (2023).

44 Cheng, S. *et al.* RGCC-mediated PLK1 activity drives breast cancer lung metastasis by phosphorylating AMPKalpha2 to activate oxidative phosphorylation and fatty acid oxidation. *J Exp Clin Cancer Res* **42**, 342, doi:10.1186/s13046-023-02928-2 (2023).

45 Pinto-Coelho, L. How Artificial Intelligence Is Shaping Medical Imaging Technology: A Survey of Innovations and Applications. *Bioengineering (Basel)* **10**, doi:10.3390/bioengineering10121435 (2023).

46 Begum, H. M. *et al.* Spatial Regulation of Mitochondrial Heterogeneity by Stromal Confinement in Micropatterned Tumor Models. *Sci Rep* **9**, 11187, doi:10.1038/s41598-019-47593-8 (2019).

47 Han, M. *et al.* Spatial mapping of mitochondrial networks and bioenergetics in lung cancer. *Nature* **615**, 712-719, doi:10.1038/s41586-023-05793-3 (2023).

48 Fischer, J. R. *et al.* Multiplex imaging of breast cancer lymph node metastases identifies prognostic single-cell populations independent of clinical classifiers. *Cell Rep Med* **4**, 100977, doi:10.1016/j.xcrm.2023.100977 (2023).

49 Jovanovic, B. *et al.* Heterogeneity and transcriptional drivers of triple-negative breast cancer. *Cell Rep* **42**, 113564, doi:10.1016/j.celrep.2023.113564 (2023).

50 Lehmann, B. D. *et al.* Identification of human triple-negative breast cancer subtypes and preclinical models for selection of targeted therapies. *J Clin Invest* **121**, 2750-2767, doi:10.1172/JCI45014 (2011).

51 Dietlmeier, J. *et al.* Few-shot hypercolumn-based mitochondria segmentation in cardiac and outer hair cells in focused ion beam-scanning electron microscopy (FIB-SEM) data. *Pattern Recognit Lett* **128**, 521-528, doi:10.1016/j.patrec.2019.10.031 (2019).

52 Gallusser, B. *et al.* Deep neural network automated segmentation of cellular structures in volume electron microscopy. *J Cell Biol* **222**, doi:10.1083/jcb.202208005 (2023).

53 Gupta, Y., Heintzmann, R., Costa, C., Jesus, R. & Pinho, E. Deep learning-enhanced automated mitochondrial segmentation in FIB-SEM images using an entropy-weighted ensemble approach. *PLoS One* **19**, e0313000, doi:10.1371/journal.pone.0313000 (2024).

54 Casser, V., Kang, K., Pfister, H. & Haehn, D. in *Proceedings of the Third Conference on Medical Imaging with Deep Learning* Vol. 121 (eds Arbel Tal *et al.*) 111--120 (PMLR, Proceedings of Machine Learning Research, 2020).

55 Gao, H. & Ji, S. in *2017 IEEE International Conference on Data Mining (ICDM)* 871-876 (IEEE Computer Society, 2017).

56 Wei, D. *et al.* MitoEM Dataset: Large-scale 3D Mitochondria Instance Segmentation from EM Images. *Med Image Comput Comput Assist Interv* **12265**, 66-76, doi:10.1007/978-3-030-59722-1_7 (2020).

57 Xu, C. S. *et al.* An open-access volume electron microscopy atlas of whole cells and tissues. *Nature* **599**, 147-151, doi:10.1038/s41586-021-03992-4 (2021).

58 Heinrich, L. *et al.* Whole-cell organelle segmentation in volume electron microscopy. *Nature* **599**, 141-146, doi:10.1038/s41586-021-03977-3 (2021).

59 Pereira, R. O. *et al.* OPA1 deficiency promotes secretion of FGF21 from muscle that prevents obesity and insulin resistance. *EMBO J* **36**, 2126-2145, doi:10.15252/embj.201696179 (2017).

60 Favaro, G. *et al.* DRP1-mediated mitochondrial shape controls calcium homeostasis and muscle mass. *Nat Commun* **10**, 2576, doi:10.1038/s41467-019-10226-9 (2019).

61 Neikirk, K. *et al.* Systematic Transmission Electron Microscopy-Based Identification and 3D Reconstruction of Cellular Degradation Machinery. *Adv Biol (Weinh)* **7**, e2200221, doi:10.1002/adbi.202200221 (2023).

62 Southard, S. *et al.* A series of Cre-ER(T2) drivers for manipulation of the skeletal muscle lineage. *Genesis* **52**, 759-770, doi:10.1002/dvg.22792 (2014).

63 Lam, J. *et al.* A Universal Approach to Analyzing Transmission Electron Microscopy with ImageJ. *Cells* **10**, doi:10.3390/cells10092177 (2021).

64 Han, J. *et al.* ER-stress-induced transcriptional regulation increases protein synthesis leading to cell death. *Nat Cell Biol* **15**, 481-490, doi:10.1038/ncb2738 (2013).

65 Sarkans, U. *et al.* The BioStudies database-one stop shop for all data supporting a life sciences study. *Nucleic Acids Res* **46**, D1266-D1270, doi:10.1093/nar/gkx965 (2018).

Figure 1

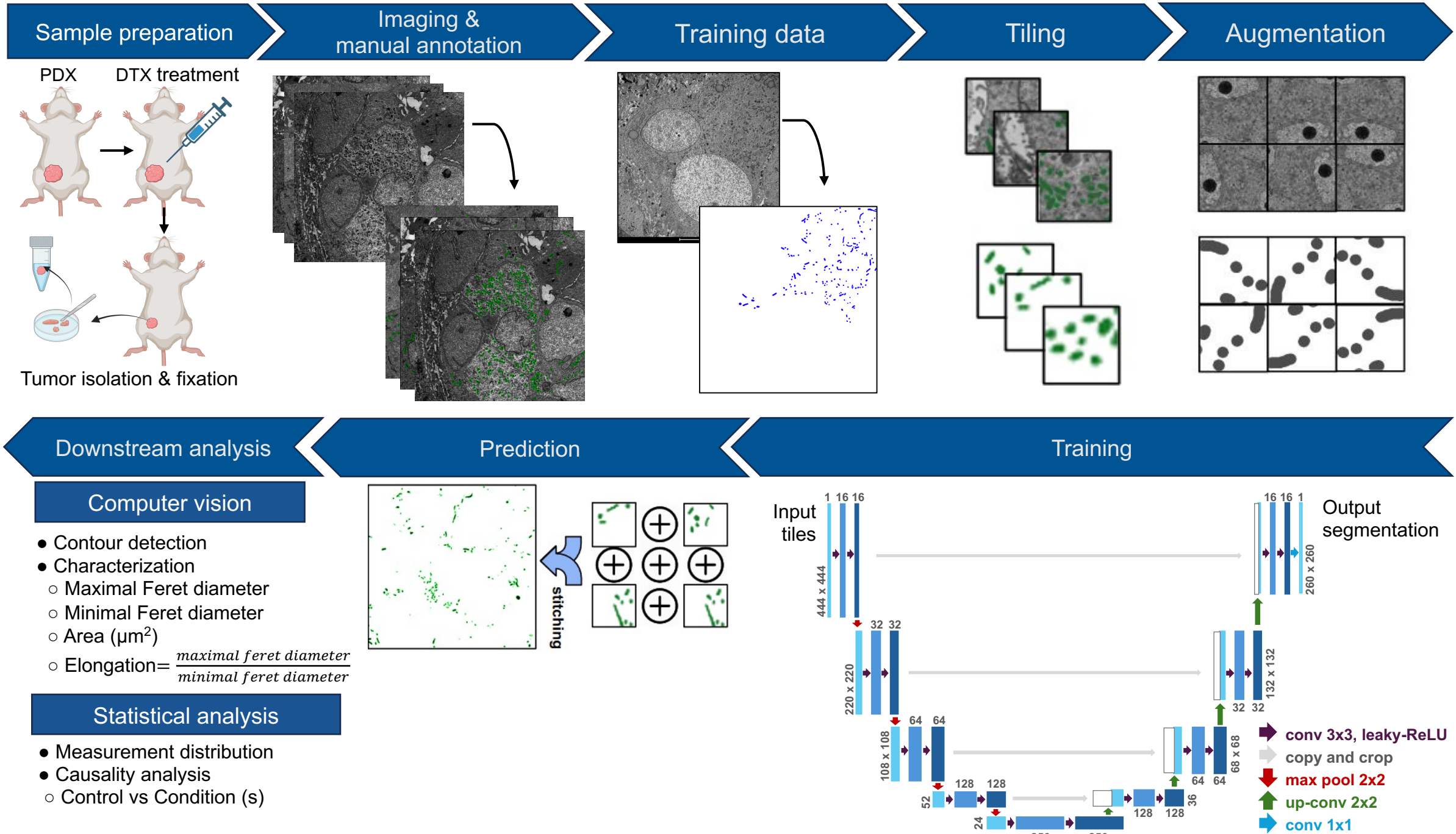
Sample preparation
Imaging & manual annotation
Training data
Tiling
Augmentation
PDX
DTX treatment
Tumor isolation & fixation
Downstream analysis
Prediction
Training
Computer vision
● Contour detection
● Characterization
○ Maximal Feret diameter
○ Minimal Feret diameter
○ Area (µm²)
○ Elongation= maximal feret diameter / minimal feret diameter
Statistical analysis
● Measurement distribution
● Causality analysis
○ Control vs Condition (s)
stitching
Input tiles
Output segmentation
conv 3x3, leaky-ReLU
copy and crop
max pool 2x2
up-conv 2x2
conv 1x1

Figure 2

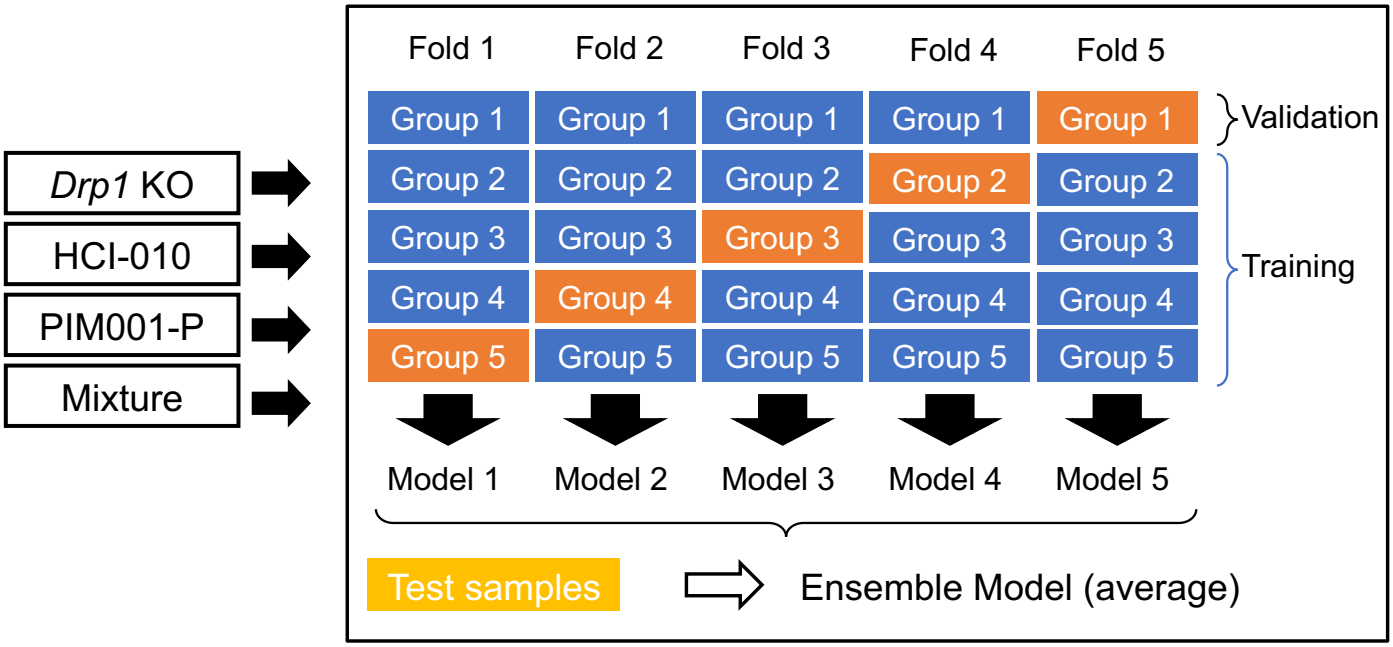
Fold 1
Fold 2
Fold 3
Fold 4
Fold 5
Drp1 KO
HCI-010
PIM001-P
Mixture
Group 1
Group 2
Group 3
Group 4
Group 5
Validation
Training
Model 1
Model 2
Model 3
Model 4
Model 5
Test samples
Ensemble Model (average)

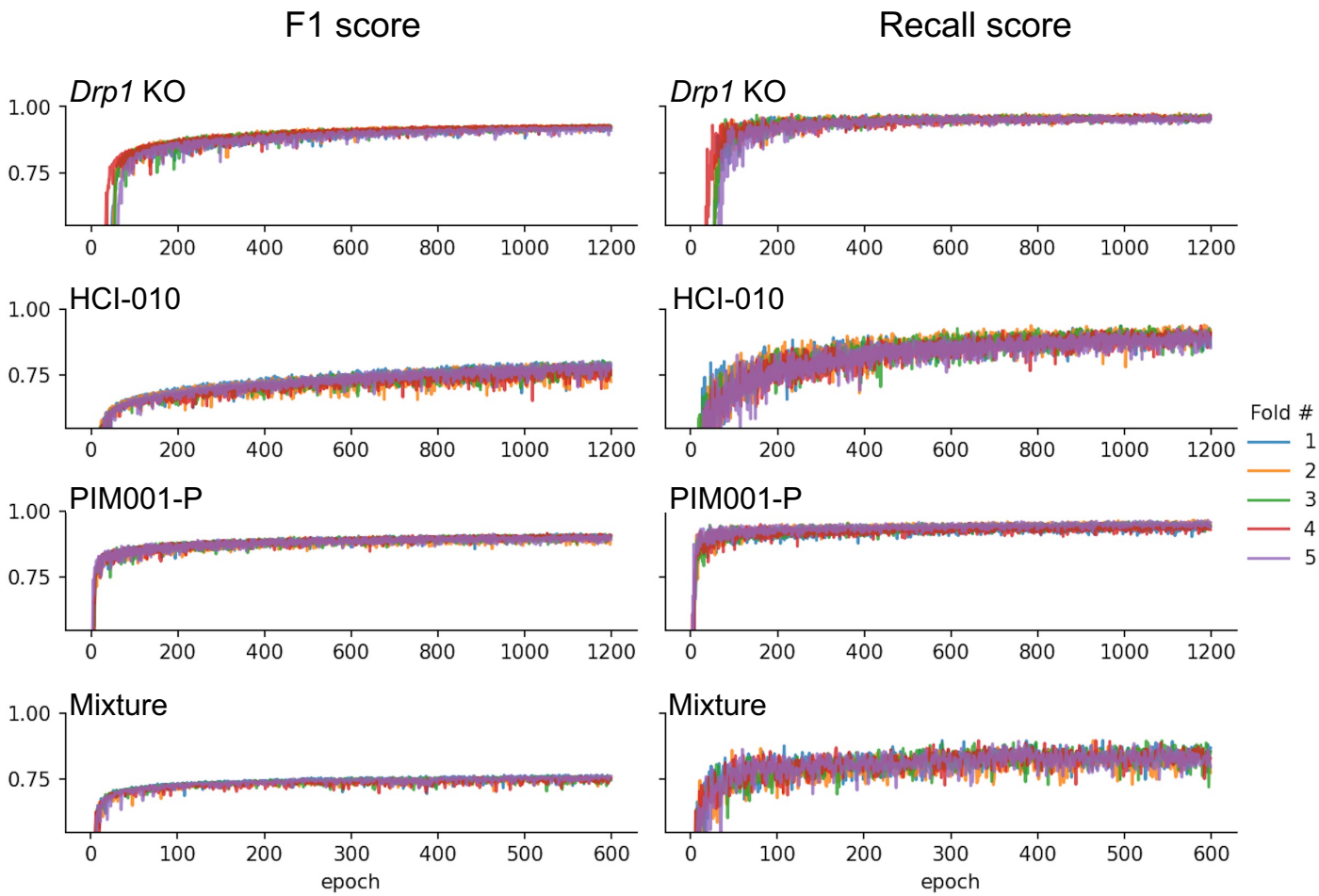
F1 score
Recall score
Drp1 KO
HCI-010
PIM001-P
Mixture
1.00
0.75
0
200
400
600
800
1000
1200
100
300
500
epoch
Fold #
1
2
3
4
5

Figure 3

A

F1 score

Test Dataset	*Drp1* KO	HCI-010	PIM001-P	Mixture	Mixture++	Mixture-RCNN	MitoNet-v1
Drp1 KO	0.84	0.52	0.56	0.80	0.79	0.59	0.78
HCI-010	0.53	0.72	0.70	0.74	0.75	0.72	0.19
PIM001-P	0.19	0.78	0.86	0.84	0.83	0.67	0.62

Training Dataset Model

Recall score

Test Dataset	*Drp1* KO	HCI-010	PIM001-P	Mixture	Mixture++	Mixture-RCNN	MitoNet-v1
Drp1 KO	0.92	0.41	0.47	0.91	0.92	0.69	0.88
HCI-010	0.41	0.89	0.79	0.74	0.83	0.85	0.12
PIM001-P	0.10	0.83	0.90	0.82	0.85	0.76	0.58

Training Dataset Model

B

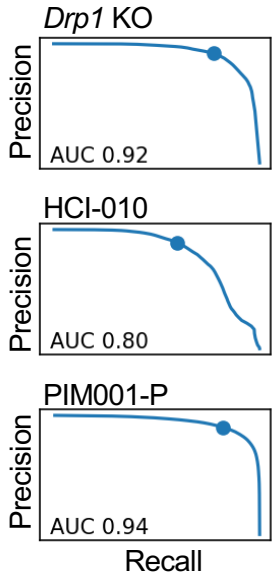

C

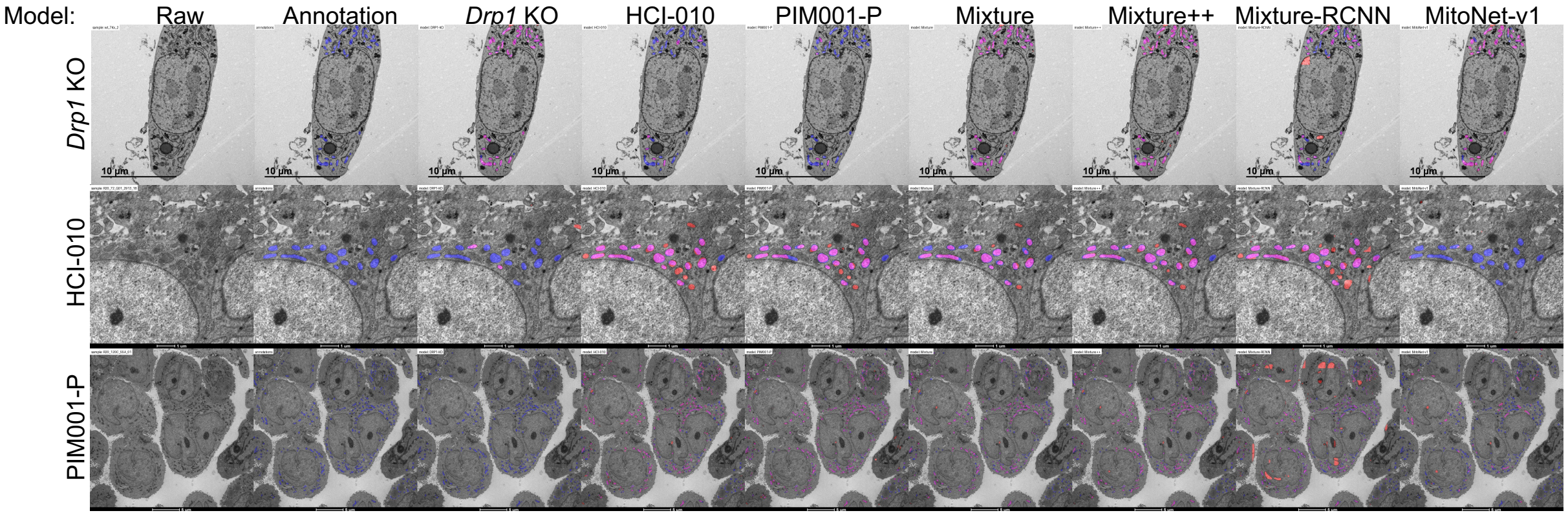

Figure 4

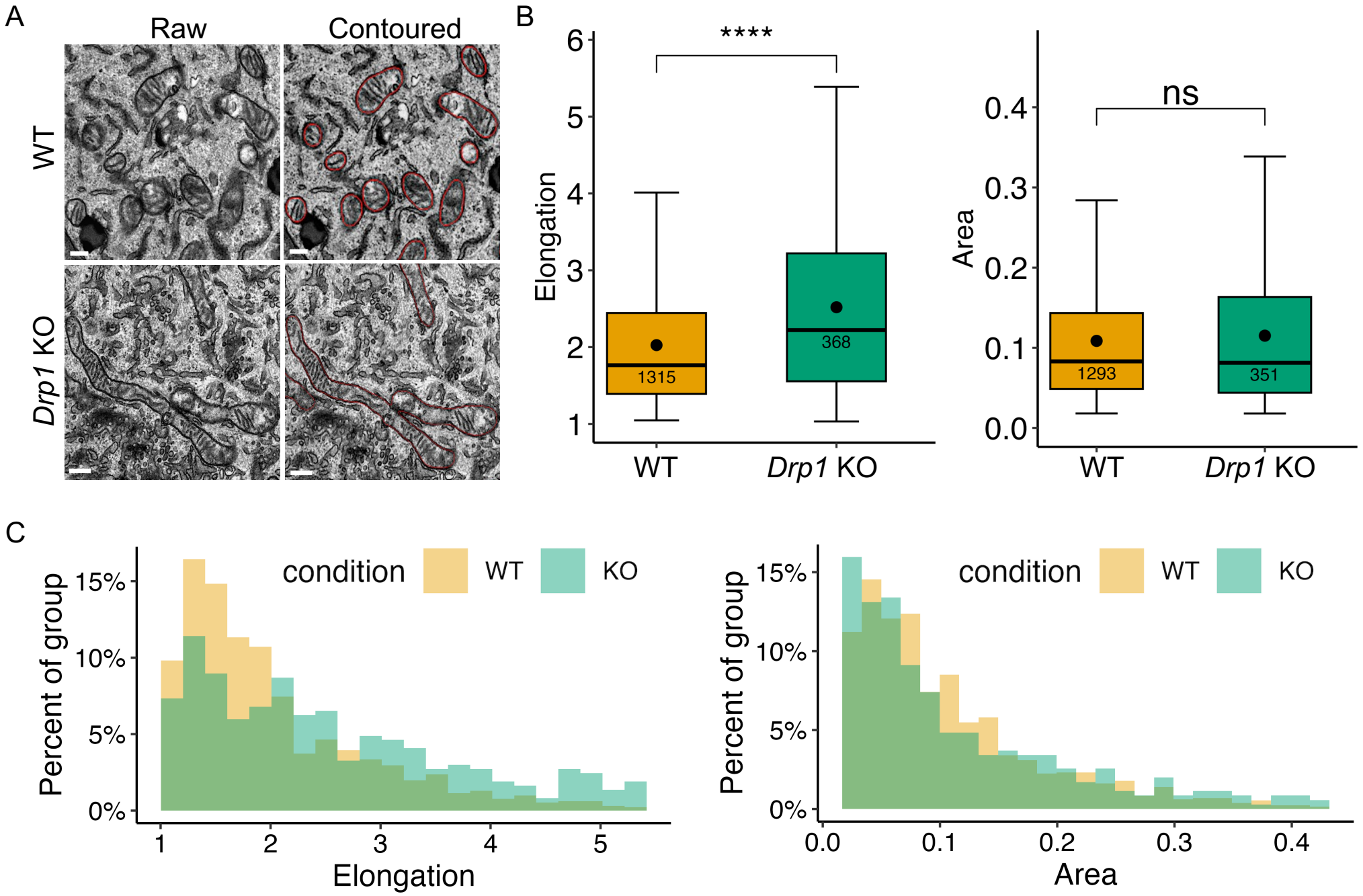
A
Raw
Contoured
WT
Drp1 KO
B
****
Elongation
1315
368
WT
Drp1 KO
ns
Area
1293
351
WT
Drp1 KO
C
condition
WT
KO
Percent of group
Elongation
condition
WT
KO
Percent of group
Area

Figure 5

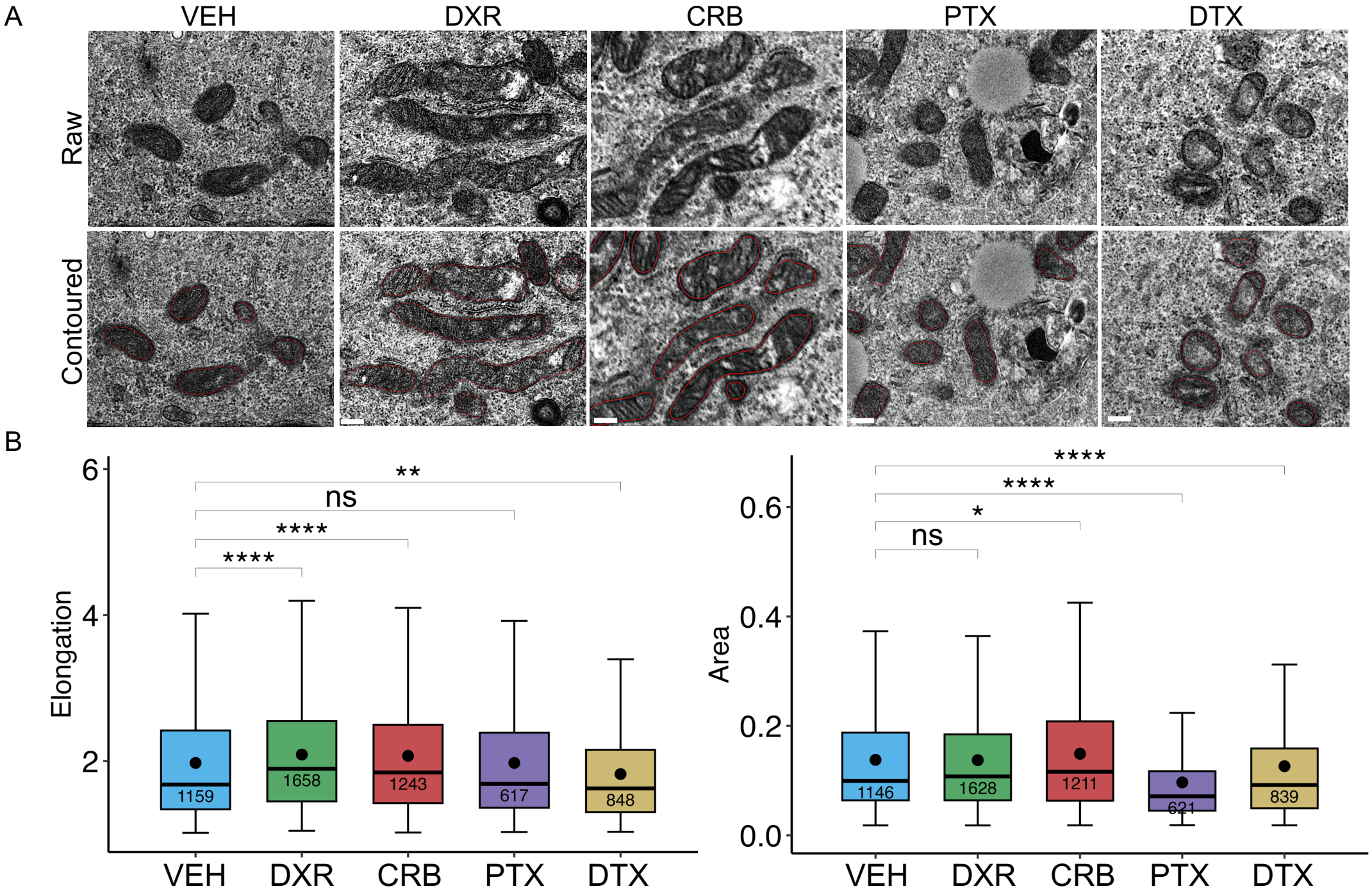
A
VEH
DXR
CRB
PTX
DTX
Raw
Contoured
B
Elongation
6
4
2
**
ns
****
****
1159
1658
1243
617
848
VEH
DXR
CRB
PTX
DTX
Area
0.6
0.4
0.2
0.0
****
****
*
ns
1146
1628
1211
621
839
VEH
DXR
CRB
PTX
DTX

Figure 6

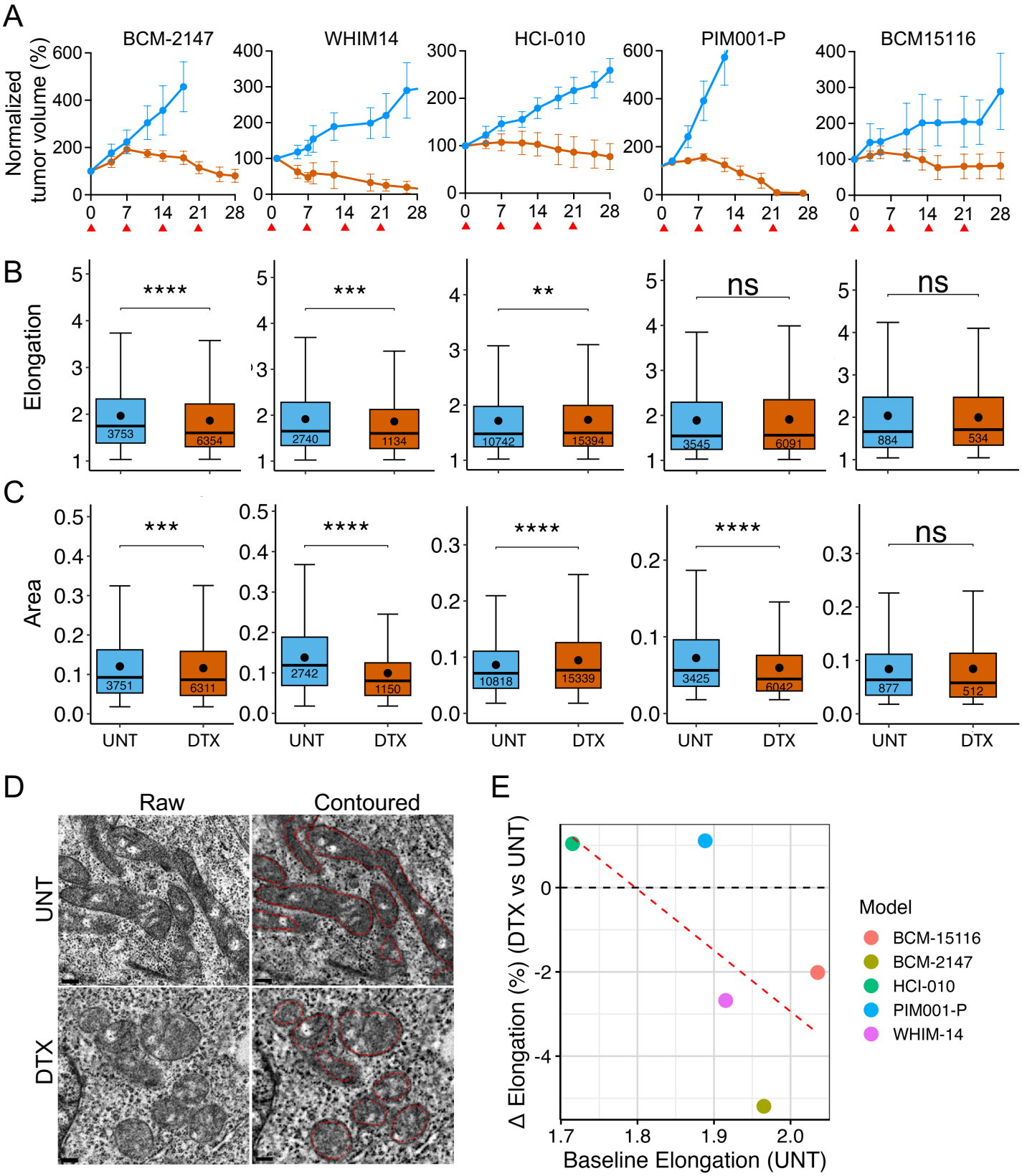
A
BCM-2147
WHIM14
HCI-010
PIM001-P
BCM15116
Normalized tumor volume (%)
B
Elongation
****
***
**
ns
ns
3753
6354
2740
1134
10742
15394
3545
6091
884
534
C
Area
***
****
****
****
ns
3751
6311
2742
1150
10818
15339
3425
6042
877
512
UNT
DTX
D
Raw
Contoured
UNT
DTX
E
Δ Elongation (%) (DTX vs UNT)
Baseline Elongation (UNT)
Model
BCM-15116
BCM-2147
HCI-010
PIM001-P
WHIM-14

Figure 7

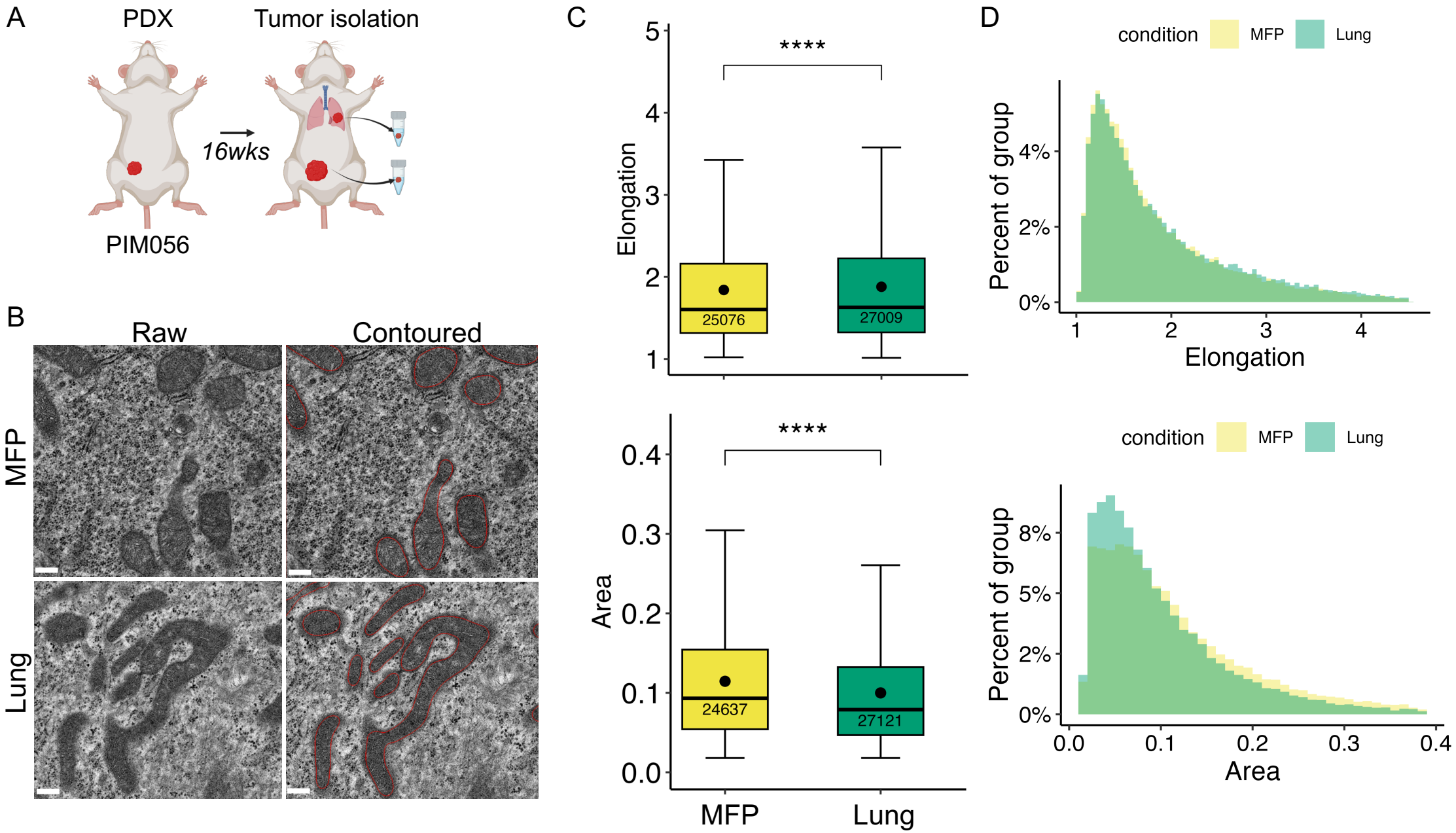
A
PDX
Tumor isolation
16wks
PIM056
B
Raw
Contoured
MFP
Lung
C
****
Elongation
25076
27009
****
Area
24637
27121
MFP
Lung
D
condition
MFP
Lung
Percent of group
Elongation
condition
MFP
Lung
Percent of group
Area
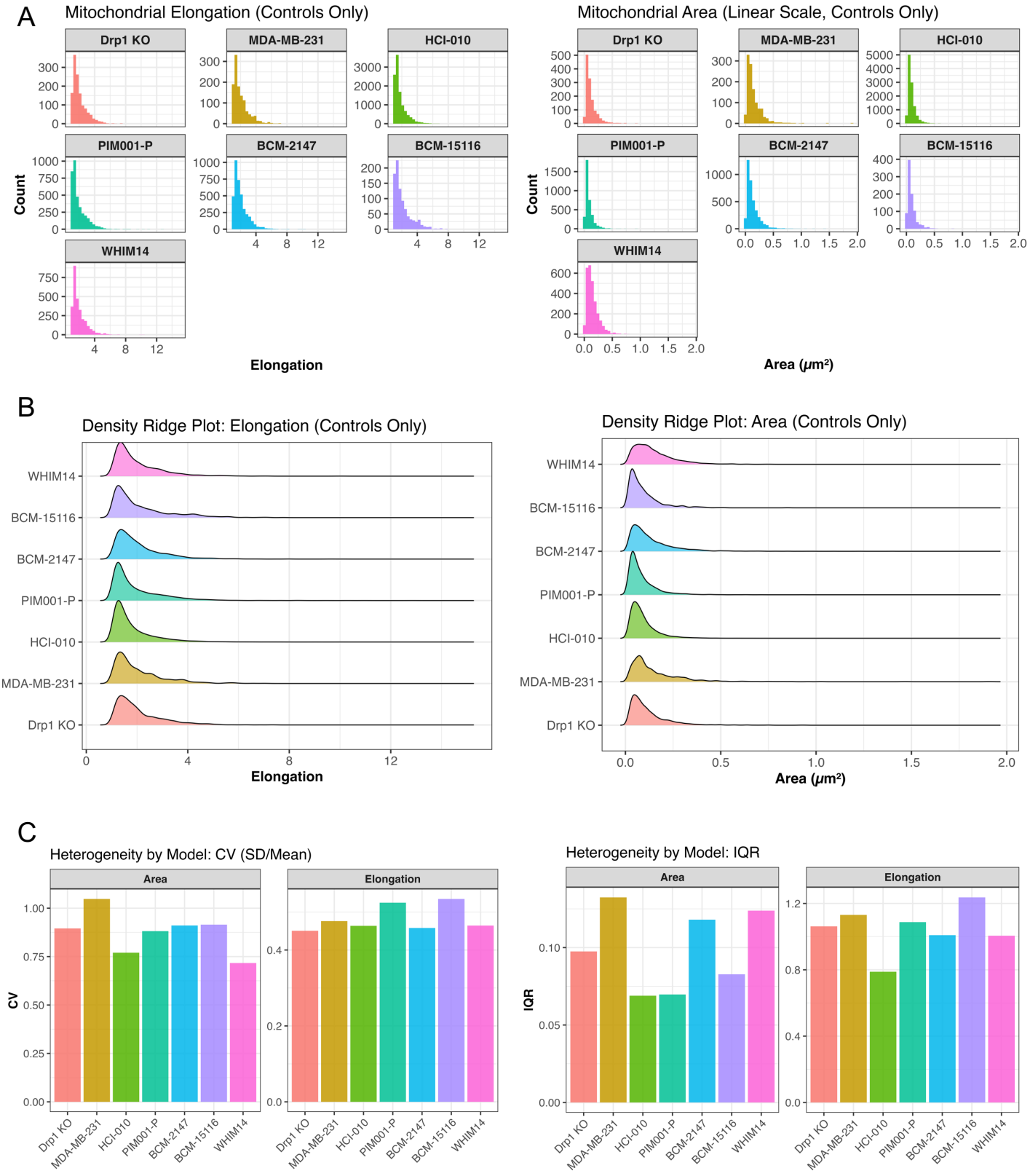
Supplementary Figure 1